

POLITECNICO DI TORINO

DEPARTMENT OF MECHANICAL AND AEROSPACE ENGINEERING

Master's Degree Course in Biomedical Engineering



In silico framework for the certification of Nitinol staples

Academic Year 2020/2021

Candidate

Dall'Omo Roberta

Supervisor

Ing. Terzini Mara

Ing. Carbonaro Dario

Prof. Audenino Alberto

December 2021

Contents

| | |
|--|-----------|
| Abbreviations..... | I |
| Introduction..... | II |
| List of figures..... | V |
| 1 Clinical Problem and Treatment Background | 1 |
| 1.1 Skeletal system anatomy | 1 |
| 1.2 Bone Fracture..... | 3 |
| 1.3 Treatment: fracture internal fixation and osteosynthesis | 5 |
| 1.4 Staple..... | 9 |
| 1.4.1 Nitinol staple..... | 11 |
| 1.4.1.1 Nitinol staple related complications..... | 16 |
| 1.5 Nitinol | 18 |
| 1.5.1 Shape memory effect | 19 |
| 1.5.2 Superelasticity..... | 21 |
| 1.5.3 Biocompatibility | 23 |
| 2 ASTM F564-17..... | 26 |
| 2.1 Introduction..... | 26 |
| 2.2 Material and mechanical property testing | 26 |
| 3 State of the art – Finite Element Models | 29 |
| 4 Materials and Methods | 33 |
| 4.1 Staple Geometry..... | 33 |
| 4.2 Staple FE Model..... | 35 |
| 4.2.1 Nitinol material parameters | 37 |

| | | |
|----------|--|-----------|
| 4.3 | FE Simulation..... | 40 |
| 4.3.1 | Verification Tests..... | 40 |
| 4.3.2 | Four-point bending standard test simulations | 42 |
| 4.4 | FE Simulations output..... | 48 |
| 5 | Results | 50 |
| 5.1 | Uniaxial Tensile Test | 50 |
| 5.2 | Staple opening..... | 51 |
| 5.3 | Results of four-point bending tests..... | 53 |
| 5.4 | Fatigue analysis..... | 59 |
| 6 | Discussion..... | 61 |
| 6.1 | Preliminary Tests | 61 |
| 6.2 | Four-Points Bending Tests..... | 62 |
| 6.2.1 | Insertion Gap | 63 |
| 6.2.2 | Device Design: Angle – Leg..... | 63 |
| 6.2.3 | Stiffness Estimation | 64 |
| 6.3 | Fatigue analysis..... | 65 |
| 6.4 | Limits of the proposed model..... | 66 |
| 7 | Conclusion and Future Developments..... | 67 |
| | References | 69 |

A mamma, babbo e Bea

ABBREVIATIONS

Af – Austenite Finish Temperature

As – Austenite Start Temperature

ASTM – American Society for Testing and Materials International

CAD – Computer aided design

FDA – Food and Drug Administration

FE – Finite Element

FEA – Finite Element Analysis

Mf – Martensite Finish Temperature

Ms – Martensite Start Temperature

MSCs – Mesenchymal Stem Cells

RF – Reaction Force

SE – Super-elasticity

SM – Shape Memory

SMA – Shape Memory Alloy

INTRODUCTION

The thesis is part of the "Nitoliera" project, a research supported by Regione Piemonte, born from the collaboration between Politecnico di Torino, LAMP Srl, AorticLab Srl, and Intrauma Spa, for the creation of a new Nitinol supply chain. LAMP is a manufacturing company that will bring the first Nitinol production line in Italy, while AorticLab and Intrauma will produce endovascular and orthopedic medical devices, respectively, using Nitinol as raw material. Politecnico di Torino will assist the entire process. In particular, this work was accomplished with the Turin-based company Intrauma. The goal of the collaboration is the creation of a Nitinol staple for bone fixation, reconstruction and fusion. Nitinol is a material with peculiar properties and, in this work, the framework developed using FE modeling provided a state-of-the-art method to evaluate the biomechanical performance of an example device providing useful information for its certification.

Fractures are the most common traumatic injuries associated to large-organs. The development of internal fixation devices such as plates, screws, pins and cerclage wires has led to improved surgical and clinical outcomes. In recent years, shape memory alloy staples have been introduced in orthopedic surgery as alternative fixation devices, with benefits in terms of time of the surgical procedure and improved bone healing. In detail, Nitinol staples dynamically adapt to changes in the bone structure and guarantee the bone-on-bone apposition during the healing process. Further studies are currently conducted to evaluate the staples design and to increase the treatment effectiveness and safety. A variety of Nitinol staples are available, but their mechanical properties compared to standard devices are not yet completely known. In this regard, Finite Element (FE)

method is a powerful tool for evaluating the biomechanical response of fixation implants under different loading conditions, thus supporting the design phase to characterize and optimize the mechanical performance. In silico modelling of standard mechanical tests plays a fundamental role in supporting the medical device development and testing, enabling to reduce time and costs compared to a pure experimental approach. Within this context, this work focuses on the development of a numerical platform to support the characterization and the regulatory submission of staple fixation devices. A FE model of the commercially available DynaNite staple (Arthrex) was implemented. The geometry of the device was resembled from literature and manufacture's specifications, 3D tetrahedral elements were adopted to realize the mesh and a super-elastic material model was implemented to characterize the mechanical behaviour of Nitinol. Within the FE framework, the ASTM F564 – 17 standard was accounted by considering two separate mechanical tests, namely the elastic bending test and the constant amplitude fatigue bending test. Accordingly, numerical simulations of the two tests were carried out, implementing an FE model of the four-point bending load apparatus, in accordance with the regulation. The load of testing machine in function of the axial displacement of the actuator and the peak value of the maximum principal strain of the staple were considered to evaluate the mechanical performance of the device. The developed FE models allow to obtain the mechanical output quantities required by the ASTM standard. In addition, the study enables to identify critical zones for the structural integrity of the device, that are not experimentally obtainable. Once validated, the model may replace the corresponding experimental tests during the device certification phase.

The thesis is organized as follow:

Chapter 1 introduces in general the concept of bone anatomy and bone fracture pathology, describing the possible treatments available for internal fixation. Then an overview on metallic bone staple is given, focused on Nitinol staples which are the topic of this work.

Chapter 2 describes the reference standard ASTM F564 – 17 for mechanical tests on metallic staple for internal fixation of the musculoskeletal system.

Chapter 3 illustrates the current state of the art in terms of FE models concerning Nitinol shape memory staple implantation simulations and device outcomes optimization.

Chapter 4 describes the methods used for the CAD model of the staple geometry and the simulations employed. The creation of the staple model was based on the geometric data collected from the literature, two-dimensional images and manufacturer information. Therefore, the four-points bending load apparatus described in ASTM F564 - 17 was implemented. Accordingly, different material properties were assigned to each component.

Chapter 5 describes the obtained results: biomechanical investigations were conducted using post-processing and comparisons employing biomechanical quantities to evaluate the mechanical performance of the device.

Chapter 6 analyses the results presented in the previews chapter with a comparison with literature.

Chapter 7 ends the thesis work, with a discussion about the advantages of *in silico* trials and a perspective for future development.

LIST OF FIGURES

| | |
|---|----|
| <i>Figure 1 – Internal structure of a human long bone</i> | 2 |
| <i>Figure 2 – Fracture healing schematic process</i> | 5 |
| <i>Figure 3 – Estimated number of fragility fractures by fracture category in 2017 and 2030</i> | 6 |
| <i>Figure 4 – Example of staple and screw fixation in foot phalanges</i> | 7 |
| <i>Figure 5 – Schematic of Screw Terms</i> | 8 |
| <i>Figure 6 – A) Smith & Nephew/Richards Regular Fixation Staple available with and without Spikes. B) Smith & Nephew/Richards Krackow HTO Staple</i> | 10 |
| <i>Figure 7 – Staple devices of Arthrex and Striker companies</i> | 10 |
| <i>Figure 8 – DynaClip Bone Fixation System®</i> | 12 |
| <i>Figure 9 – DePuy Synthes (Johnson & Johnson) staple's devices</i> | 13 |
| <i>Figure 10 – DynaNite staple and delivery device</i> | 14 |
| <i>Figure 11 – Insertion in the bone with NiTi compression staple</i> | 15 |
| <i>Figure 12 – Patient presenting with a non-union and a broken staple across the third TMT joint.</i> | 17 |
| <i>Figure 13 – Crystal transformation of Nitinol SMA</i> | 19 |
| <i>Figure 14 – Mechanism of SME when test temperature is below M_f</i> | 20 |
| <i>Figure 15 – Tensile behaviour of stainless steel and Nitinol (schematic)</i> | 21 |
| <i>Figure 16 – Mechanism of superelasticity when test temperature is above A_f</i> | 22 |
| <i>Figure 17 – Temperature-dependent stress and strain curves for SMA materials</i> | 23 |
| <i>Figure 18 – Staple in Four-Points Bending Load Apparatus</i> | 27 |
| <i>Figure 19 – Sample implementation steps for trans-sternal closure using Nitinol staples</i> | 31 |
| <i>Figure 20 – DynaNite Nitinol Staple, 25 mm x 20 mm, AR-8719-2520</i> | 33 |
| <i>Figure 21 – Main dimensions of the staple device</i> | 34 |
| <i>Figure 22 – The Staple FE model with a focus on critical zones</i> | 37 |
| <i>Figure 23 – Superelastic behavior of Nitinol (UMAT Abaqus routine)</i> | 38 |

| | |
|--|-----------|
| <i>Figure 24 – Three-dimensional beam mesh for tensile test.</i> | <i>41</i> |
| <i>Figure 25 – Schematic view of the two loading conditions.</i> | <i>41</i> |
| <i>Figure 26 – Generic view of simulation step of staple opening.</i> | <i>42</i> |
| <i>Figure 27 – ASTM Preliminary Tests. A) Staple in standard configuration with an insertion gap of 2 mm. B) Staple in standard configuration completely inserted.</i> | <i>44</i> |
| <i>Figure 28 – ASTM Final Tests. A) Staple in standard configuration with an insertion gap of 2 mm. B) Staple in standard configuration completely inserted. C) Staple in open configuration completely inserted.</i> | <i>45</i> |
| <i>Figure 29 – Staple in Four-Point Bending Load Apparatus Scheme of Numerical Simulation.</i> | <i>46</i> |
| <i>Figure 30 – Stress vs Strain response for uniaxial tensile stress showing the superelastic effect of the material.</i> | <i>50</i> |
| <i>Figure 31 – Superelastic behaviour of Nitinol (with a focus on model parameters chosen)</i> | <i>51</i> |
| <i>Figure 32 – Curves of Reaction Force developed for each leg versus the displacement and Bending Moment comparison.</i> | <i>51</i> |
| <i>Figure 33 – Maximum Principal Stress contour plots and relative stress-strain curve for the two configurations of staple opening.</i> | <i>52</i> |
| <i>Figure 34 – Results of Applied Force and Bending Moment for the two configurations.</i> | <i>54</i> |
| <i>Figure 35 – Contour Plots of the last geometry: Maximum Principal Stress on the left and Maximum Principal Strain on the right.</i> | <i>55</i> |
| <i>Figure 36 – Maximum Principal Stress and Strain curves for the highest stressed element for the two set up configurations.</i> | <i>55</i> |
| <i>Figure 37 – Results of Applied Force and Bending Moment for the three configurations.</i> | <i>57</i> |
| <i>Figure 38 – Max. Principal Stress and Strain of the highest stressed element.</i> | <i>58</i> |
| <i>Figure 39 – Numerical results obtained for the strain constant life diagram.</i> | <i>60</i> |
| <i>Figure 40 – Contour plots of Von Mises Stress of a complete inserted staple (on the right) and a gap of 2 mm (on the left).</i> | <i>63</i> |
| <i>Figure 41 – Force-displacement curve with stiffness estimation.</i> | <i>65</i> |

1 CLINICAL PROBLEM AND TREATMENT

BACKGROUND

1.1 Skeletal system anatomy

Orthopaedics is the branch of surgery that deals with the diseases and correction of deformities of the musculoskeletal system. The musculoskeletal system includes bones, cartilage, ligaments, tendons and connective tissues. Its main functions include supporting body weight, protecting vital organs, enabling movement, and maintaining the posture. Orthopaedic surgeons use both surgical and non-surgical means to treat musculoskeletal trauma, spinal disorders, sports injuries, degenerative diseases, tumours and congenital disorders.

The human skeleton provides a framework for muscles and other soft tissues. It is composed of about 270 bones at birth and 206 bones in adulthood, after some bones get fused together. The skeletal system has several functions, including support, movement, protection, mineral homeostasis, blood-cell formation and triglyceride storage [1]. Bones are made up of different shapes and have complex internal and external structures that can reduce weight while remaining hard. Living bone is white in color and consists of compact or cortical bone on the outside and spongy or trabecular bone on the inside; the latter is characterized by a honeycomb structure. In mature bone, the trabeculae are arranged in an orderly pattern that forms continuous units of bone tissue aligned parallel to the lines of the greatest compressive or tensile forces. The arrangement of the trabeculae provides maximum stiffness with minimum use of material. The internal structure of the bone is shown schematically in *Figure 1*.

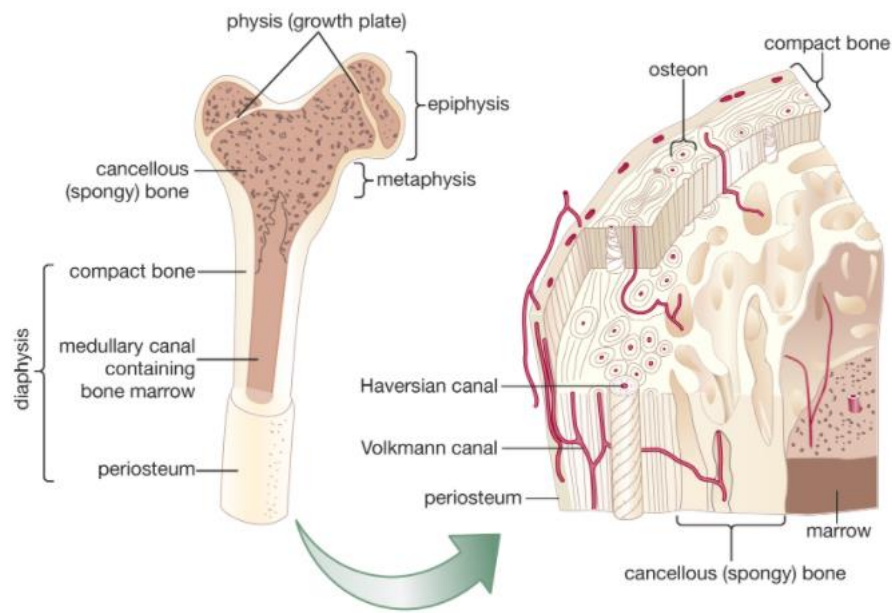


Figure 1 – Internal structure of a human long bone. Figure is taken from [2]

Bones generally contain mineralized extracellular matrix in which a number of specialized cells, such as osteoblasts, osteoclasts, and osteoclasts are embedded [3].

Bone matrix has three main components:

- 20-30% organic matrix (osteoid)
- 60-70% inorganic mineral content (mineral salts)
- 10-20% water

Bone hardness depends on the type and amount of minerals available to the body.

Hydroxyapatite is one of the main minerals present in bones.

Bone and bone marrow are highly vascularized and this vascular network accounts for about 10-20% of cardiac output [4]. The blood vessels in bone are necessary for almost all skeletal functions, including the supply of oxygen and nutrients, homeostasis and repair. If the blood supply to the bone is interrupted, this can lead to the death of bone tissue (osteonecrosis).

1.2 Bone Fracture

Once bone has formed and matured, it undergoes constant remodelling by osteoclasts and osteoblasts, replacing old bone tissue with a new one. Resorption of the extracellular matrix by osteoclasts is followed by an osteoblastic invasion of the cavity and subsequent secretion of the extracellular matrix. These sequential processes occur continuously and in a balanced relationship and are referred to as bone remodelling. Optimal remodelling is responsible for bone health and strength throughout life [5]. When a fracture occurs, bone remodelling is involved in the process of bone repair. When an implant is needed, the goal is to aid the bone formation process with a strong fixation of the implant to the bone.

A bone fracture is an interruption in the continuity of a bone. A significant percentage of fractures occur as a result of high force impact or stress. However, a fracture may also be caused by certain conditions that weaken the bones, such as osteoporosis and some cancers (namely pathological fracture). More than 1.5 million fractures per year are due to osteoporosis [6]. Osteoporosis is defined as a skeletal disease characterized by a loss of bone mass and a reduction in bone density that impairs bone strength and leads to an increased risk of fracture. The most common sites for fragility fractures are the hip, distal radius, spine, proximal humerus, and ankle. In most cases, surgical intervention followed by rehabilitative treatment is required [7]. The clinical relevance of osteoporosis lies in the associated fragility fractures; until such an event occurs, there are usually no symptoms. In the Western world, approximately 1 in 3 women and 1 in 5 men over the age of 50 will experience a fracture during their lifetime. After the age of 50 years, most fractures can be considered characteristic of osteoporosis [8].

The healing process of bones is a complex process in which both medicine and mechanics play an important role and can influence the timing of the healing process. All broken bones go through the same healing process: inflammation, bone repair, new bone formation and remodelling.

- *Inflammatory phase.* The inflammatory response is essential to the beginning of fracture healing. It begins at the moment the bone is broken and lasts for about five days [9]. A hematoma is formed, which is a source of hematopoietic cells capable of secreting growth factors. The damaged bone tissue on the sides of the fracture fragments dies and therefore the dead cells release chemicals called cytokines that initiate the healing process [10]. Fibroblasts and mesenchymal cells migrate to the fracture site and between four and ten days after the fracture, a tissue called granulation tissue forms (*Figure 2A-C*).

- *Bone repair phase.* Following inflammation, vascular remodelling (angiogenesis and neovascularization) begins with the recruitment of mesenchymal stem cells (MSCs). Subsequently, many of the MSCs that formed the fibrovascular callus differentiate into either osteoblasts or chondrocytes to initiate bone formation [10]. A soft callus (a type of soft bone) replaces the blood clot that formed in the inflammatory stage (*Figure 2D-E*). Over the next few weeks, the soft callus becomes harder.

- *Remodelling phase.* The remodelling phase begins about 6 weeks after injury and may even last for several years. The bone that was originally formed is replaced with mature lamellar bone. Bone is absorbed where it is not needed by osteoclasts and formed by osteoblasts where it is needed. Over time, the remodelling process restores the bone to its traditional shape (*Figure 2F*).

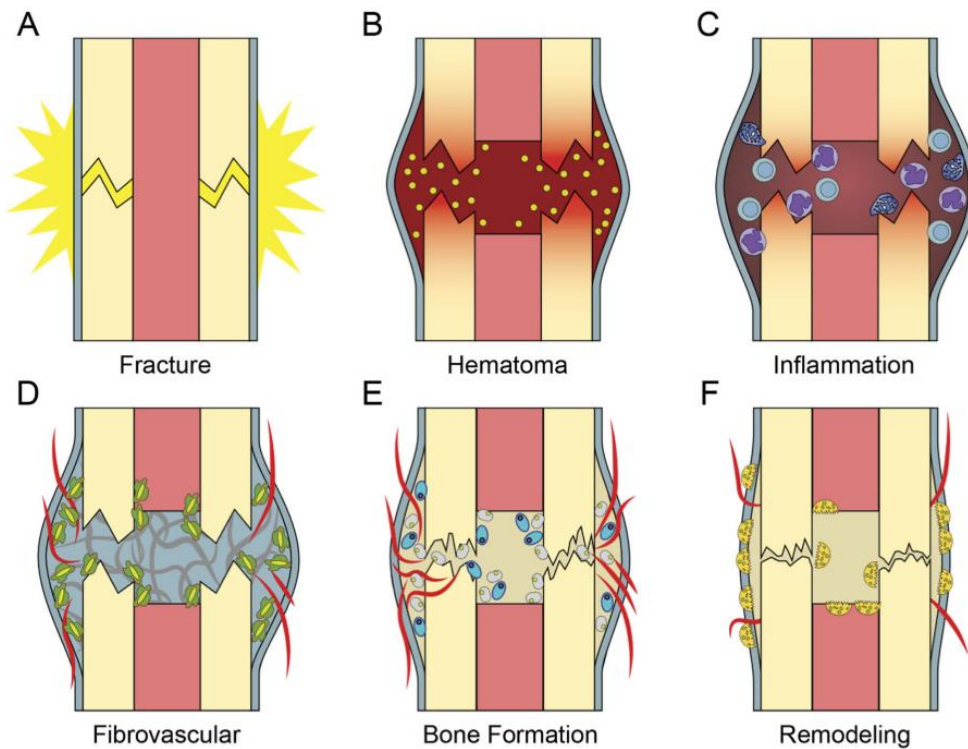


Figure 2 – Fracture healing schematic process. Figure taken from [10].

1.3 Treatment: fracture internal fixation and osteosynthesis

Several studies have been conducted on the incidence of fractures in relation to age or disease, most based on data from hospital databases. In the United States, approximately 6.3 million fractures occur each year, of which approximately 1.5 million are due to bone disease [11]. In Europe, the total number of fragility fractures is expected to increase from 2.7 million in 2017 to 3.3 million in 2030, that means a 23% increase (*Figure 3*) [8].

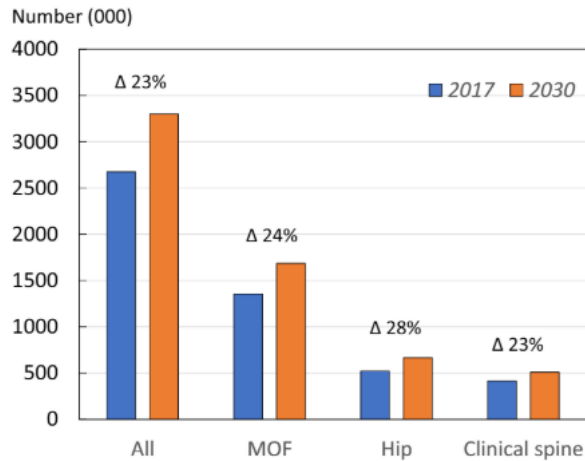


Figure 3 – Estimated number of fragility fractures by fracture category in 2017 and 2030. Numbers denote the percentage change for all fragility fractures, major osteoporotic fracture (MOF), hip and clinical spine fractures.

Figure is taken from [8].

Fractures impose both short- and long-term costs on health care sector and society. Many fractures are treated non-operatively, but many of them require surgical treatment. The basic goal of fracture fixation is to stabilize the fractured bone, allow rapid healing and restore mobility and full function of the injured extremity. Orthopedic implants are widely used in the clinic because they could play a good role in fixation and replacement in the treatment of orthopedic diseases [12]. In the field of internal fixation, osteosynthesis is one of the most common operative techniques in orthopaedic surgery. It consists of the union of two or more bone fragments after their proper alignment has been previously gained [13].

Numerous devices are used to mechanically stabilize the fracture, either alone or in combination with other devices (an example is shown in *Figure 4*). The main ones are classified into the following major categories: wires, pins and screws, plates, and intramedullary nails or rods, staples and clamps [14][15]. Currently, most implants for internal fixation are made of stainless steel, titanium or, more recently, nitinol.



Figure 4 – Example of staple and screw fixation in foot phalanges. Figure is taken from [16].

Nowadays, screws (*Figure 5*) are the most commonly used in orthopaedic surgery and in many cases are applied as primary internal fixation devices [13]. They are used both as stand-alone fixations and in conjunction with other orthopaedic devices, especially plates [17]. The geometric parameters of the screws affect the mechanical performance, especially the pull-out strength. The main complication of these devices is that screw loosening might be a common problem in the fixation of bone fractures and that the stress shielding around the screw threads is partially responsible for excessive bone absorption [18].

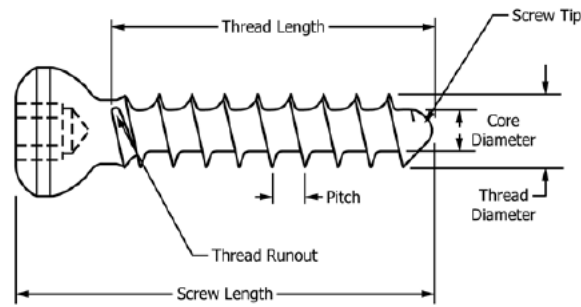


Figure 5 – Schematic of Screw Terms. Figure is taken from [19].

Screws are often used to ensure the assembly of plates and the bone. Plates are devices that provide an artificial shaft for the alignment of two displaced bone fragments. Treatment of a large number of fractures relies on this concept, but sometimes plate fixation may be too rigid and interfere with the natural process of bone remodelling [13]. The disadvantages of plate fixation include the risk of re-fracture of the bone after its removal, stress protection and osteoporosis beneath a plate, plate irritation and, in rare cases, an immunological reaction [14].

Another traditional technique for fracture fixation involves the use of Kirschner wires, which were first introduced in 1909 [20]. K-wires are sterilised, sharpened, smooth stainless-steel pins and are used alone or more commonly in combination with other orthopaedic fixation devices. There are several complications with these devices, such as heat generation during insertion, infection, loss of fixation and even migration of K-wires to another site of the implant can occur [14][16].

Because of the complications that arise with many of the most commonly used fixation devices, metallic staples can be a useful tool in fixation techniques. The use of staples for these types of procedures has several advantages, including easier fixation to

the bone, avoidance of infection issues, the ability to provide additional compression unlike K-wires and their lower profile compared to a larger plate [16].

1.4 Staple

As mentioned above, the advantages of staple fixation may include good approximation of fragments, dynamic compression, avoidance of pin tract infection from exposed hardware, and technically shorter operative time compared to bone screws [21]. A bone staple is conceptually a single fixation device consisting of 2 or more entry points into the bone (named legs) that are joined together.

Metallic bone staples are widely used in hand, foot, and ankle surgery and they have been used in the United States since 1906 [22][21]. In the classic application, a staple device is simply inserted into the bone to stabilize a fracture or osteotomy and promote bone healing. Staples may be used as an adjunct to other forms of fixation or as a single or multiple fixation device in one location.

Various types of bone staples are available, differing in their shape and physical properties. Devices made of stainless steel or cobalt chrome are the first used and the most consolidated. *Smith & Nephew, (United Kingdom)* [23] offers a complete family of fixation staples with distinct design advantages, such as Richards staple model and Krackow HTO Staple (*Figure 6*). For these kinds of devices, compression is achieved by the mechanical properties of the staple and no further compression is achieved once the staple is inserted into the bone [24].

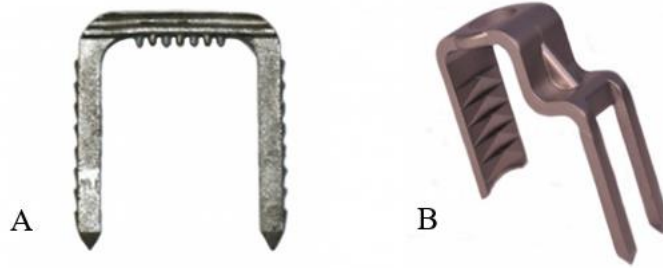


Figure 6 – A) Smith & Nephew/Richards Regular Fixation Staple available with and without Spikes. B) Smith & Nephew/Richards Krackow HTO Staple. Figures taken and adapted from [25].

Thanks to their versatility, variety of shape and size, capability to be used not only for bone fixation but also for bone-soft tissue fixation, many companies have started investing and producing these devices. *Arthrex (Florida, USA)* is provided by QuickFix staple system (*Figure 7*) made of stainless steel with a size of 8 and 10 mm in wide and 1 mm in diameter. *Stryker Corporation (Michigan, USA)* offers a variety of models, some of them are shown in *Figure 7*, made of Vitallium alloy (65% cobalt, 30% chromium, 5% molybdenum, and other substances).



Figure 7 – Staple devices of Arthrex and Striker companies. Pictures are taken from company's websites and brochures.

Despite the quick and less traumatic surgical procedure and ergonomic design, the staples mentioned above share some common disadvantages. Stainless steel staples manifest a high stiffness and a permanent deformation after bending, which is disadvantageous for an optimal result of the surgical procedure [24]. In general, traditional bone staples have demonstrated an inconsistent quality of fixation, tendency to loosen, lack of compression and bulkiness, as found in some mechanical tests, in vitro and in vivo models, and clinical follow-up [22] [26] [27].

1.4.1 Nitinol staple

Currently, to avoid the drawbacks of the traditional devices used until now and to improve the stability and performance of the staples, in the last few decades it started to produce staples from a metal composition of nickel and titanium called Nitinol. Nitinol is an acronym that stands for nickel (Ni), titanium (Ti), and Naval Ordnance Laboratory (NOL). It is a nickel-titanium metal alloy characterized by superelastic and shape memory properties (see *chapter 1.5*). These implants are suitable for the generation of continuous interfragmentary compression with the aim of primary bone healing. Conventional stainless steel or titanium orthopedic implants have a limited capacity to store or release energy and are less effective or difficult to employ [28].

The NiTi compression staple was introduced in China and first used in the human body in 1981 [21] [29]. The first commercial Nitinol staples were released to the Chinese market in 1981, to the European market in 1990, and in the US market in the mid-1990s [29]. In 1987, Yang and colleagues reported the first clinical investigation of fracture fixation using nitinol staples. They documented 51 procedures for fractures and

arthrodesis and described good bone union and functional recovery in the 45 cases that were followed up [30].

Nowadays, the production of this type of devices is constantly increasing, with new shapes and structures being tested. The main companies that have obtained FDA (Food and Drug Administration) approval for their devices are the following reported.

- *MedShape (Atlanta, USA)*
 - **DynaClip Bone fixation system® (Figure 8)**

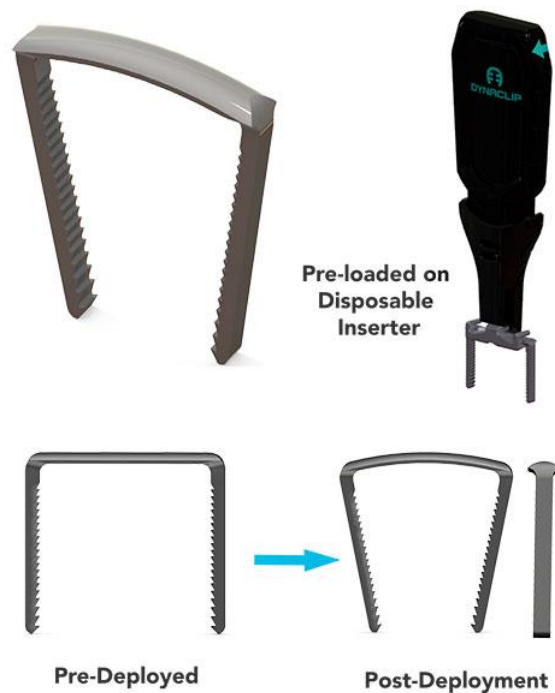


Figure 8 – DynaClip Bone Fixation System®. Figure is taken from the webpage [31].

- *DePuy Synthes (Johnson & Johnson)*
 - **SPEEDTITAN™ Continuous Compression Implant System** (staple available with different length of the leg and bridge), see *Figure 9A*
 - **BME Speed Implant™** (4-legs or 2-legs configuration), see *Figure 9B*
 - **SPEEDTRIAD™ Continuous Compression Implant System**, see *Figure 9C*

▪ **Hammertoe Continuous Compression Implants, see Figure 9D**

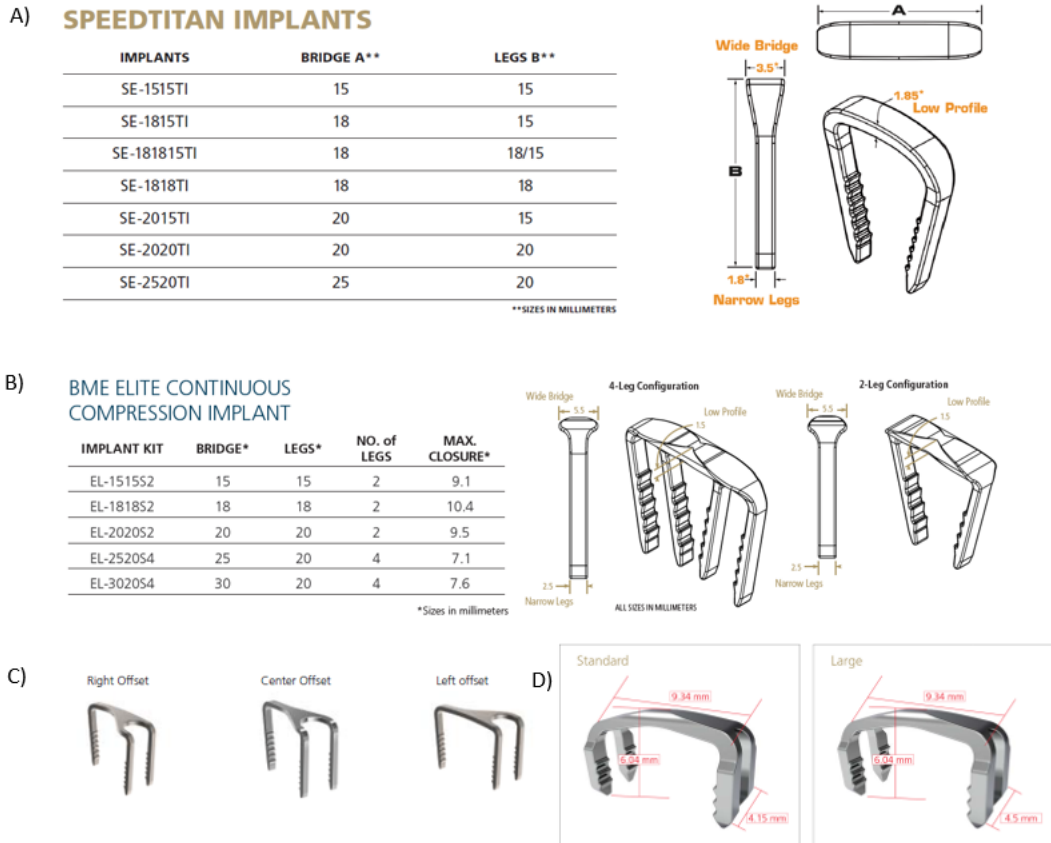


Figure 9 – DePuy Synthes (Johnson & Johnson) staple's devices. Figures are taken from company's brochures.

• *Arthrex (Florida, USA)*

- **DynaNite®**: the implant is available in single-use sterile kits. Ergonomically designed DynaNite delivery device allows the surgeon to control the opening of the staple legs *Figure 10*.



Figure 10 – DynaNite staple and delivery device. Figure is taken from brochure.

Despite the variety of models available on the market, nitinol staples have generally been shown to be safe implants and are comparable to stainless steel and titanium fixation devices [29]. Although the clinical applications of SMA staples are multiple and include use as compressive devices for fixation of osteotomies, arthrodesis of small bones, and fixation of fractures, clinical studies are limited. A study by T. C. Mereau and colleagues [21] treats the use of nitinol staples on 31 feet in 27 patients who underwent arthrodesis or an osteotomy and shows that compression staples provide an adequate source of internal fixation in foot surgery. In addition, a study by Tang et al [32] on 36 metatarsal osteotomies for hallux valgus fixed with NiTi staples showed a shortened bone healing time in patients.

With a typical Nitinol bone staple, holes are predrilled in the bone, an “open” Nitinol staple is inserted into the holes, and the staple recovers either super-elastically or by shape memory to pull the fractured bones together and apply a compressive force to the fracture surfaces (see *Figure 11*).

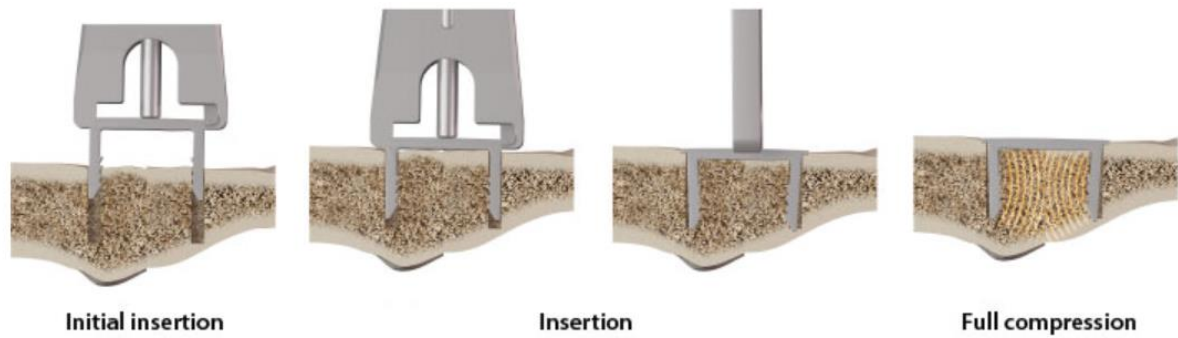


Figure 11 – Insertion in the bone with NiTi compression staple. Figure is taken from [33].

Different staple designers and manufacturers have achieved this basic approach in different ways. Basically, there are three classes of NiTi staples, depending on the property they exhibit [34].

- **Room Temperature Superelastic (SE):** the austenite finish (A_f) transformation temperature is near or below room temperature and the staple must be held open by some type of device before implantation. This type of staple will attempt to close at any temperature at or above room temperature once the constraint is removed.
- **Body Temperature Activated (BT):** this type of Nitinol staple has an A_f temperature below body temperature but above room temperature. Shape recovery is triggered by the thermal shape memory effect when the staple reaches body temperature. In this case, it is important to maintain the temperature of the staple below body temperature during insertion to prevent premature deployment.
- **Heat Activated (HA):** this category of Nitinol staple has an austenite start (A_s) temperature near body temperature and an A_f temperature low enough to allow deployment without the application of excessive heat, in order to prevent tissue

damage. These staples can be activated by the application of heat by a cautery device or by using an external controlled heat source.

To date, there are not enough studies to state which typology is optimal in terms of performance and healing. For more details about A_s and A_f see *Chapter 1.5*.

1.4.1.1 Nitinol staple related complications

The most common complications after staple implantation include loss of fixation, breakage and rarely migration. Studies have shown that the stability of staple fixation depends on leg length and width, cross-sectional geometry, insertion angle and also bone density [21][35].

To prevent loss of fixation, barbed staples have been developed. In addition, double staple constructs have been shown to improve stability as demonstrated by Q. Hoon et al. in their biomechanical study [36], in which they compared the results obtained when inserting a single or two perpendicular staples in polyurethane blocks construct loaded in four-points bending.

Since these are compression devices that exert compressive forces on the implant site, it is important to optimise these forces because excessive strength can cause pressure necrosis and prevent healing, while if insufficient can slow healing and may even allow fracture recurrence [34]. There are also limitations to the use of staples in very compromised osteoporotic bone or highly fragmented fractures. Galvanic corrosion is also a problem that needs to be considered, as staples can be used in the same fixation construct with other fixation devices made of dissimilar metals [28].

A recent study on tarsometatarsal (TMT) arthrodesis conducted by C. Dock et al [37] focused on the use of BME compression staple on sixty-six patients (68 feet). The results show that the average time to fusion, as determined by radiographs, was 8.4 weeks and no wound complications occurred. Indications for subsequent surgeries (26.5%, 18/68 feet) included pain (n = 14), broken staples and non-union (*Figure 12*).



Figure 12 – Patient presenting with a non-union and a broken staple across the third TMT joint. Figure taken from [37].

In summary, there is enormous potential for the employment of nitinol staples in the orthopaedic field, but there is limited research available on the use of these devices and how they compare to currently available implants as a form of fixation.

1.5 Nitinol

As mentioned above, Nitinol is a metal alloy in which the two elements nickel and titanium are present in nearly equiatomic percentages. The specific term is derived from the words "Nickel Titanium Naval Ordnance Laboratory," where the alloy was first researched. While conducting research at the Naval Ordnance Laboratory in 1959, William J. Buehler, a metallurgist expert in intermetallic alloys, along with Frederick E. Wang, discovered for the first time the properties of a nearly equiatomic mixture of nickel and titanium [38].

This alloy exhibits unique properties, such as superelasticity (or pseudoelasticity) and shape memory. The properties of nitinol arise from its ability to undergo reversible, thermomechanically induced phase transformation. The dynamic reversibility of the crystallographic structure of the 2 solid phases (the parent and secondary phases) leads to the unique shape memory effect, superelasticity and high damping properties of Nitinol [38] [39].

The parent phase, called *austenite*, has a B2 body-centered cubic crystal structure; austenite is an atomically ordered solid state that is mainly stable at high temperatures. The secondary or daughter phase, called *martensite*, is characterized by a monoclinic B19' crystal structure (*Figure 13*) and is stable at low temperatures [40]. Nitinol exhibits a nonlinear behavior, in which the martensite - austenite reversible transformation is characterized by a hysteresis cycle.

The Nitinol material is characterized by the following transition temperatures [38]:

- A_s is the temperature at which the austenitic transformation begins.
- A_f is the temperature at which the austenitic transformation ends.

- M_s is the temperature at which the martensitic transformation begins.
- M_f is the temperature at which the martensitic transformation ends.

Thermoelastic martensitic phase transformation can be triggered either by temperature or by a stress state.

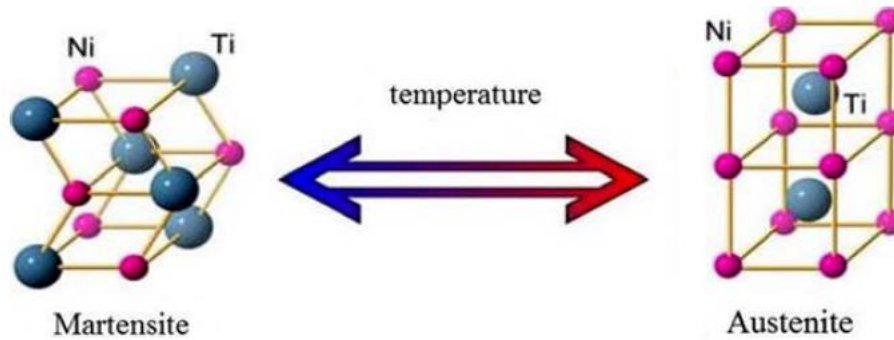


Figure 13 – Crystal transformation of Nitinol SMA. Figure taken from [41]

1.5.1 Shape memory effect

Shape memory behaviour is a direct response of the austenite - martensite phase transformation. In general, shape memory alloys exhibit the ability to recover their original shape.

Initially, the lattice structure adopts the atomically ordered body-centered cubic arrangement characterized by the austenite phase and is memorized in the set shape [38]. The parent austenite phase is stable above austenite finish temperature and when nitinol is cooled to a temperature below the martensite finish temperature (M_f), the atoms undergo diffusionless transformation by rearranging within the crystals into various complex three-dimensional structures, particularly a twinned oriented martensitic phase [38] [42].

To better appreciate the shape memory effect, the material is in a martensitic state at test temperature. When we apply an external force, martensite changes to detwinned

martensite, in which that the crystallographic orientation is aligned with the direction of the force. After the stress is removed, the material becomes in a detwinned martensitic state. When we heat this material above the austenite finish temperature (A_f), reverse transformation occurs from detwinned martensite to parent phase and the original shape is recovered. This is the mechanism of the shape memory effect (SME). The mechanism of SME is shown in *Figure 14*.

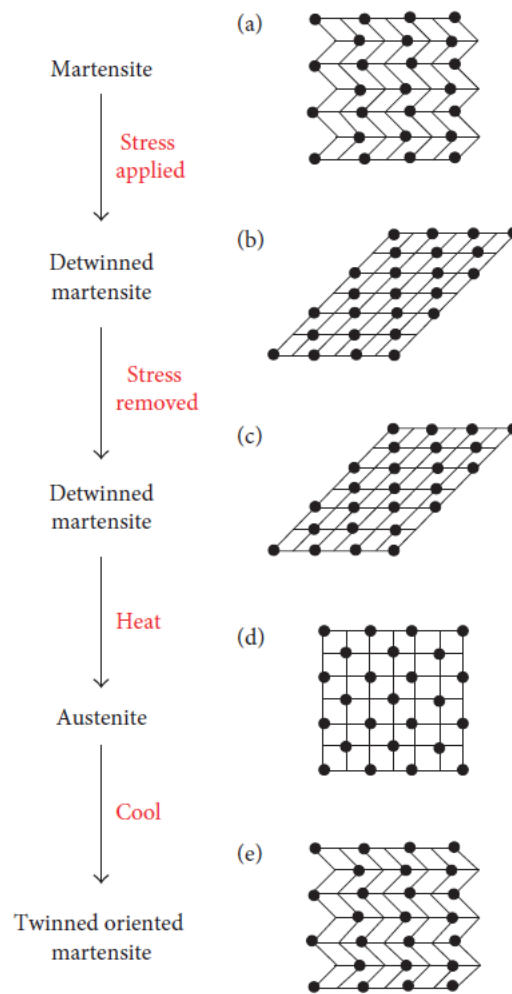


Figure 14 – Mechanism of SME when test temperature is below M_f . (a) Martensite at test temperature. (b) Detwinned martensite upon application of stress. (c) Detwinned martensite upon removal of stress. (d) Austenite upon heating above A_f . (e) Martensite upon cooling below M_f (test temperature). This figure was taken from [42].

1.5.2 Superelasticity

Superelasticity refers to the enormous elasticity of these alloys and this characteristic is very interesting for the industry and medical application. Nitinol alloys' flexibility can be up to 10 times greater than stainless steels (SS) used in medicine today and follows a non-linear path characterised by a marked hysteresis [43] [44], how it is schematically reported in *Figure 15*.

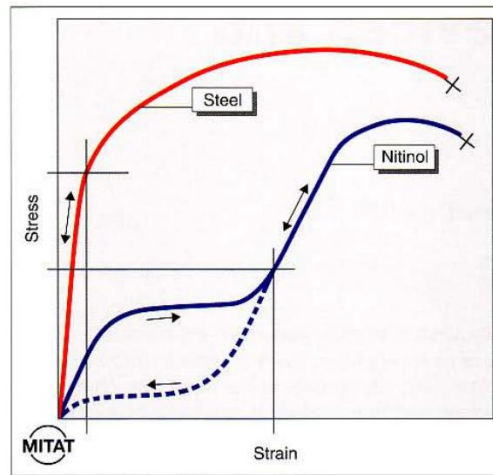


Figure 15 – Tensile behaviour of stainless steel and Nitinol (schematic). This figure was taken from [43].

The mechanism of superelasticity is shown in detail in *Figure 16*. At a constant temperature higher than A_f , the material is in the austenite phase. A stress application induces a transformation to the detwinned martensite phase, characterized by a large degree of strain with small increases in stress. The material is deformed such that the crystallographic orientation is aligned with the direction of the stress. When the stress is removed, the material reverts back to austenite with complete recovery of the original shape configuration.

In case of superelasticity, heating is not required to recover the original shape as here martensite is stable only under the application of stress [38] [42].

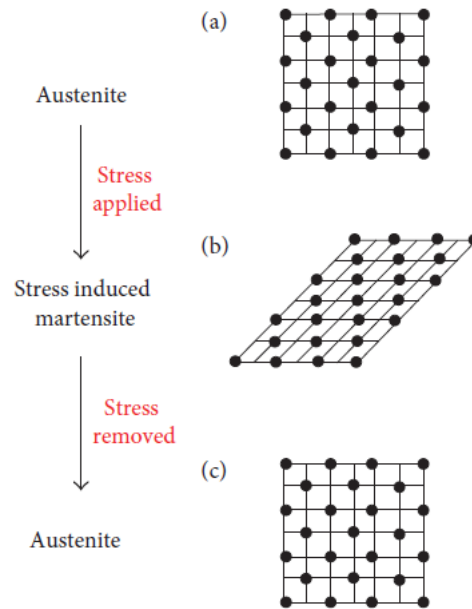


Figure 16 – Mechanism of superelasticity when test temperature is above A_f . (a) Austenite at test temperature. (b) Stress induced martensite upon application of stress. (c) Austenite upon removal of stress. Figure taken from [42].

In summary, temperature-dependent stress and strain curves for SM and SE materials are reported in *Figure 17*.

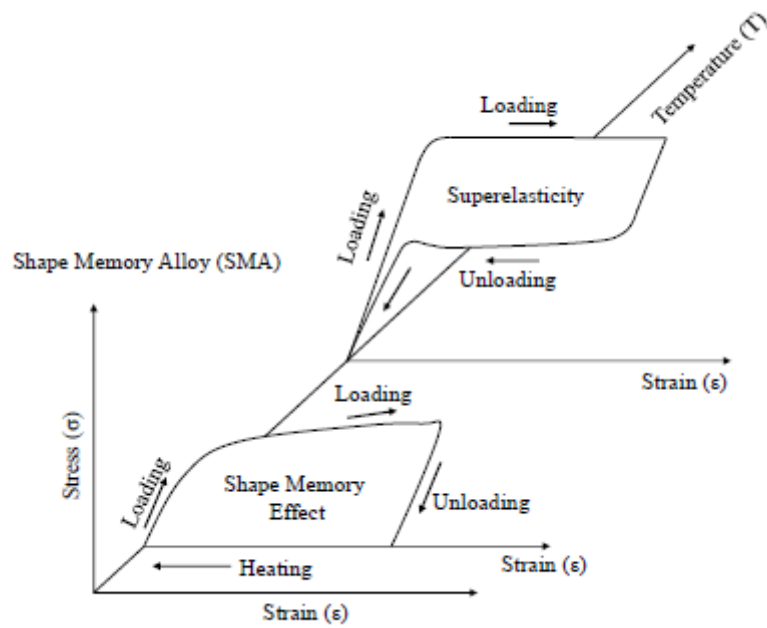


Figure 17 – Temperature-dependent stress and strain curves for SMA materials. Figure was taken from [45].

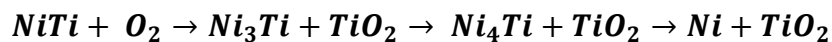
1.5.3 Biocompatibility

Due to their unique properties, Nickel-Titanium alloys are rapidly becoming one of the best biomaterials for innovative medical devices, such as self-expanding stents, grafts, staples, support systems, filters and various other devices for minimally invasive interventional and endoscopic procedures [46].

The potential danger of nitinol is related to the negative effects of the release of nickel ions into the human body. Nickel is a toxic element that primarily causes contact allergies. The prevalence of nickel allergy in the European population is about 8% to 19% in adults and 8% to 10% in children and adolescents, with a large preponderance of women [47]. For good biocompatibility, nitinol should have good corrosion resistance, so the release of nickel should be minimal. Moreover, the release of nickel ions due to corrosion may even affect the mechanical integrity of the device.

The FDA Guidance document “*Technical Considerations for Non-Clinical Assessment of Medical Devices Containing Nitinol*” [48] in **Section C** provides a regulation on corrosion testing for Nitinol medical devices: it is recommended that pitting corrosion tests be performed in accordance with ASTM F2129 “*Standard Test Method for Conducting Cyclic Potentiodynamic Polarization Measurements to Determine the Corrosion Susceptibility of Small Implant Devices*” or galvanic corrosion tests described in ASTM F3044 “*Standard Test Method for Evaluating the Potential for Galvanic Corrosion for Medical Implants*”. If the nitinol implant does not meet the specified acceptance criteria for corrosion resistance or does not employ an established surface finishing process, it is suggested nickel ion release testing reported in ASTM F3306 “*Standard Test Method for Ion Release Evaluation of Medical Implants*”.

To better evaluate the issue of corrosion of a device, it is recommended also to evaluate the oxidation rate of Nitinol and the formation of oxides. The phase transformation for oxidized NiTi occurs as follow [49]:



The formation of a thin film of TiO_2 is observed, which acts as a protective oxide layer. In fact, the main purpose of the processing techniques is to produce a thick, uniform, stable and highly adherent TiO_2 layer, in order to prevent the release of Ni and improve biocompatibility. In summary, Nitinol is increasingly used in medical devices because it offers good biocompatibility and excellent mechanical stability, which is achieved by proper control of all manufacturing parameters, including surface finishing

processes, in parallel with its unique thermoelastic properties and shape memory behaviour.

2 ASTM F564-17

2.1 Introduction

ASTM F564-17 “Standard Specification and Test Methods for Metallic Bone Staples” was taken as the reference standard for the device considered within this thesis. This specification covers the characterization of the design and mechanical function of metallic staples used in the internal fixation of the musculoskeletal system [50]. The standard provides guidelines for performing the following four mechanical tests:

- *Test Method for Constant Amplitude Bending Fatigue Tests of Metallic Bone Staples*
- *Test Method for Pull-Out Fixation Strength of Metallic Bone Staples*
- *Test Method for Soft Tissue Fixation Strength of Metallic Bone Staples*
- *Test Method for Elastic Static Bending of Metallic Bone Staples*

In this work, *in silico* models of the first and fourth tests were performed, to evaluate the mechanical behavior of the staple when subjected to loading cycles in a four-points bending machine.

2.2 Material and mechanical property testing

The purpose of *Constant Amplitude Bending Fatigue Tests* and *Elastic Static Bending Tests* is to determine the mechanical performance and bending rigidity of bone staples when are tested under bending loads. The four-points bending load apparatus reported in the standard is shown in *Figure 18*.

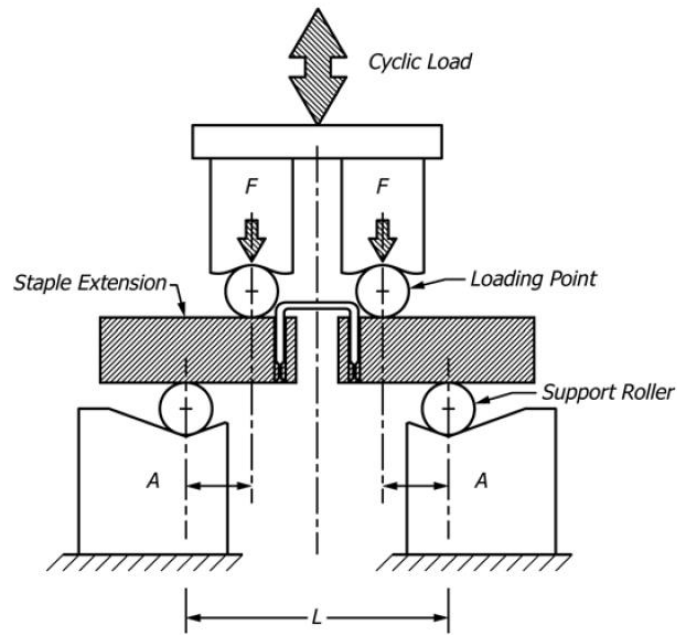


Figure 18 – Staple in Four-Points Bending Load Apparatus [50].

The apparatus is composed by:

- *Two staple extensions*: pairs of specially designed metal blocks that permit the holding of individual staples for the application of bending loads. The staple is fixed securely in the block using a moldable filling or grouting agent.
- *Four-point bend fixture*: a standard or modified bending fixture that produces pure bending in the staple, used to apply load to the staple through the extensions. It is equipped with two lower supports rollers and two upper loading rollers.

The load of the testing machine is considered in function of the axial displacement of the actuator and the bending moment to evaluate the mechanical performance of the device.

The standard indicates to compute the bending moment as follow:

$$M_{bending} = FA$$

where F is the force applied at each loading point and A is the distance between the loading point and support roller.

During fatigue tests, the specimen is subjected to cyclic loads (e.g. sinusoidal, sawtooth) until it fails or a predetermined number of cycles have been applied. Tests may be conducted at ambient conditions or in aqueous or physiological solutions at $37 \pm 2^\circ\text{C}$.

3 STATE OF THE ART – FINITE ELEMENT MODELS

The promising results obtained with the use of Nitinol staples have led to an increase in the demand for these devices in various bone fixation procedures, resulting in a multitude of staple designs. In this context, ASTM F564 – 17 "Standard Specification and Test Methods for Metallic Bone Staples" [50] defines the characterization of the design and mechanical function of metallic staples used in internal fixation of the musculoskeletal system. Although the standards define test methods for measuring the mechanical properties of metallic bone staples, experimental and computational models can be developed to better characterize current nitinol devices, optimize staple performance and material parameters.

Given the recent widespread use of these devices and the lack literature evidences, numerical and experimental simulations should be conducted to close this gap. Indeed, the effectiveness of the treatment depends largely on the design of the device and the implantation procedure. Computational modelling and engineering analysis can be applied in this field to provide additional information about the mechanical properties and the optimization of the geometry to avoid complications and postoperative behaviour.

Until now, numerical models are used to better understand the SMA and superelastic behaviour of the device and to evaluate the force generation of the shape memory devices. Finite element analysis (FEA) can significantly reduce testing and development phase time by allowing designers to develop and simulate products prior to prototype fabrication [51].

In general, there is a lack of literature regarding both computational and clinical studies of Nitinol staples. About computational studies, there are works that focus on *in*

vitro tests and optimization of the device design, while others on the surgical procedures. In particular, *Table 1* reports the current literature and modelling approaches aiming to study the mechanical behaviour and to optimize the staple design.

Table 1 - Summary of FE simulation of nitinol staples literature.

| <i>Work</i> | <i>Solver</i> | <i>Type</i> | <i>Note</i> |
|-------------------------|---|--|---|
| Hatira et al. 2012 [51] | Abaqus | SM model (developing a user subroutine UMAT) | Termomechanical loading and use the body temperature activation scheme for the staple |
| Saleeb et al. 2015 [52] | Abaqus | SM and SE model | Termomechanical loading and use the body temperature activation scheme for the staple |
| Subasi et al. 2020 [53] | Ansys | SE model | Computational sternal loading using multiple staple that is comparable to an in vitro lateral loading setup |
| Christ et al. 2009 [54] | - | SM and SE model | Termomechanical loading and use the body temperature activation scheme for the staple |
| Krone er al. 2005 [55] | Program FEAP (R.L. Taylor at the UC Berkeley) | SM and SE model | Termomechanical computational loading supported by experimental test |

SM = shape memory; SE = super elastic

FE modelling provides an useful tool for a better quantitative understanding of the biomechanical properties of the medical devices. Due to the complex physical interactions during a surgical procedure, computational modelling and engineering analysis can also be applied to evaluate and predict the long-term behaviour of staples.

Moreover, FE method can also be adopted by clinicians to predict the postoperative device performance and the potential complications, as illustrated in the most recent study of Subasi et al. [53] in which numerical analyses are carried out to optimize stapling procedure for trans-sternal closure (see *Figure 19*).

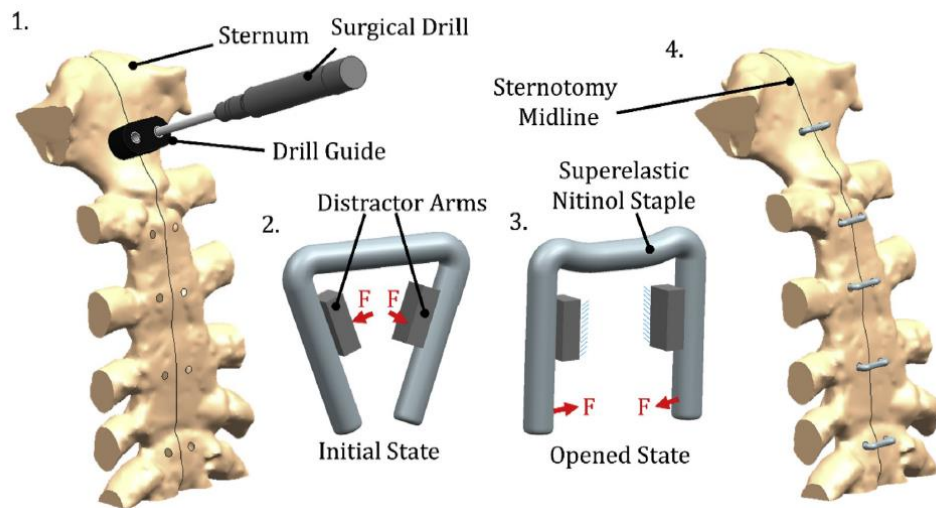


Figure 19 – Sample implementation steps for trans-sternal closure using Nitinol staples. Figure is taken from [53].

Overall, FE analyses aim to achieve an optimal staple design, even when different material properties are chosen and the real surgical procedure is mimicked. Works such as [52] and [54] investigate the shape memory effect (SME) of their model and the postoperative interaction with bones by evaluating the strain and normal stress, considering temperature changes and the contact forces developed after staple heat activation.

For instance, results obtained with FEA can be compared in conjunction with some biomechanical studies on Nitinol staples [24] [36] [56] [57] to better investigate the behaviour of the device under loading.

In summary, the studies mentioned treat staples characterized by a simple two-legged conformation (without any barbes or fillets) and are focused on optimising the design and material parameters; others on finding the best surgical approach and predicting the future evolution after implantation, also in conjunction with experimental biomechanical studies.

4 MATERIALS AND METHODS

4.1 Staple Geometry

In this work, the geometrical model of a 25x20 mm staple was created resembling the commercial device *AR - 8719-2520 - DynaNite Nitinol Staple* (Arthrex, Florida, USA) shown in *Figure 20*. The main dimensions of the staple are and show in *Figure 21*.



Figure 20 – DynaNite Nitinol Staple, 25 mm x 20 mm, AR-8719-2520. Figure taken from company's website [58].

The geometry was recreated using *Solidworks v.2020* software (Dassault Systèmes). Given the symmetry of the device, the model was reduced to an half and then mirrored in the lateral plane (*Figure 21A*). In order to obtain more accurate results and to achieve a closer compliance with the real commercial device, details such as leg barbes and fittings (rounded edges) have been maintained in the final geometric profile (*Figure 21B*).

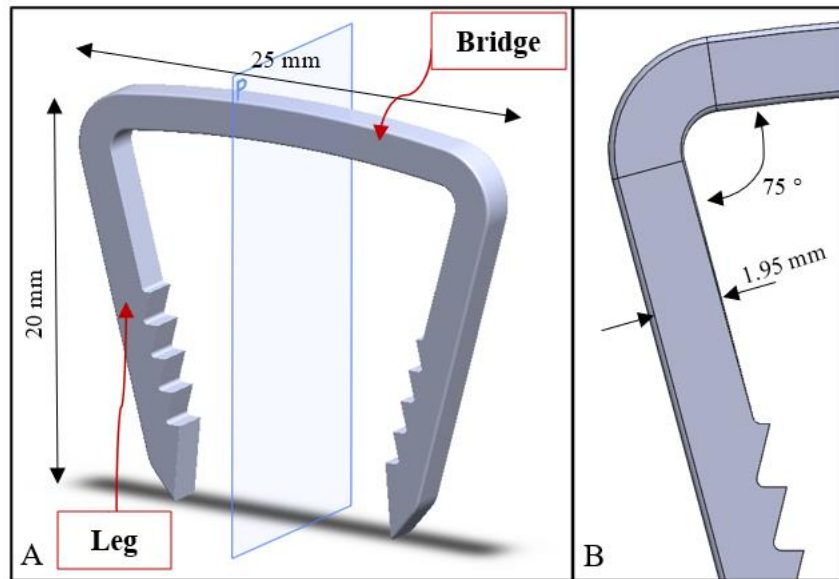


Figure 21 – Main dimensions of the staple device. A) Length of bridge and legs. B) Details about width, angle, fitting and leg barbes.

Finally, the model was exported in “*.stp” format and imported in the pre-processor *Hypermesh 2021.1* (Altair Engineering, USA) to mesh the geometry, in conjunction with *ABAQUS Standard* (Dassault Systemes Simulia Corp., Providence, RI, USA).

4.2 Staple FE Model

A tetrahedral mesh was created selecting four-node linear tetrahedral elements C3D4 (see Abaqus Documentation, Elements Guide), basing the choice on previous works [51][53][54], which model the geometry of the device with tetrahedral and hexahedral elements. Herein, tetrahedral elements were used to correctly reproduce the geometry of the device.

Using the command “*automesh*”, setting an appropriate element size, a 2D triangular mesh has been automatically created on the surface of the staple. To obtain an appropriate quality index of the mesh, manual modifications was carried out, such as setting node density on the lines, removing duplicate nodes and edges, adjusting elements size and angle in critical areas of the model, for the elements that are reported as not optimal. Mesh size was decreased at the fittings and geometrical critical zone, in order to obtain an accurate result in terms of tensions and deformations in these zones of the model. The average shell element size was 0.18 mm. Therefore, the complete three-dimensional mesh was created with “*tetramesh*” tool. To check a proper mesh frame, an element quality check was performed; the most crucial quality criteria for tetrahedral elements is the *tet collapse*, which was set to 0.2.

In summary, the checks carried out in the meshing procedure were the following:

- ***Edges***: to identify the free edges present in the model and link any surfaces that are not connected.
- ***Connectivity*** and ***duplicates***: to test the connectivity of a group of elements and verify the presence of double elements.

- **Jacobian**: measures the deviation of the element from its ideal shape. This value varies from 0 (total deformation) to 1 (coincidence with the perfect shape).
- **Minimum interior angle**: set to 15° for trias elements.
- **Maximum interior angle**: set to 130° for trias elements.
- **Tet collapse**: set to 0.2 for tetrahedron 3D elements. This parameter indicates defect generated when the height of tetrahedron 3D element is less than the target element length. Mathematically it is calculated with the following formula:

$$\mathbf{Tet\ collapse} = \mathbf{min} \left(\frac{\left(\frac{h}{\sqrt{A}} \right)}{1.24} \right)$$

where “h” represents the height between a node and the opposite face and “A” represents the area of the opposite face.

The final staple FE model is composed by 199728 elements and 40627 nodes and it is showed in *Figure 22*.

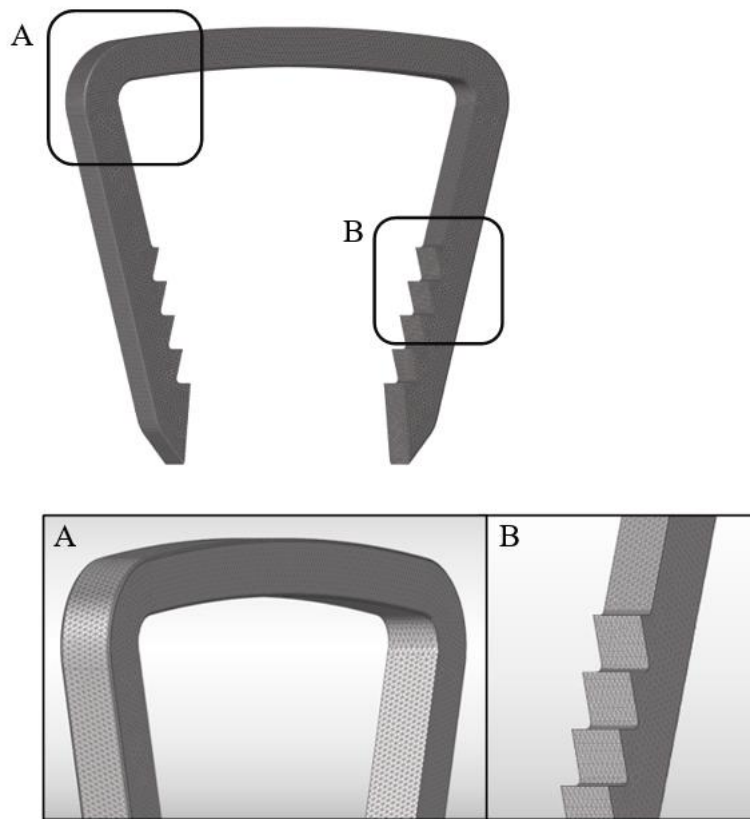


Figure 22 – The Staple FE model with a focus on critical zones.

4.2.1 Nitinol material parameters

To reproduce the Nitinol material superelasticity features, the superelasticity model provided in Abaqus [59] was implemented, based on an user-defined material subroutine (UMAT) following the model proposed by Auricchio and Taylor [60] [61].

The superelastic model is based on the uniaxial stress-strain response of phase transforming materials. Such materials are in the austenite phase under no loading conditions; austenite is assumed to follow isotropic linear elasticity. On loading the material, the austenite phase starts transforming into martensite beyond a certain stress, martensite phase is also linear elastic but with a different elasticity constant. Upon unloading, the transformation is reversible (*Figure 23*).

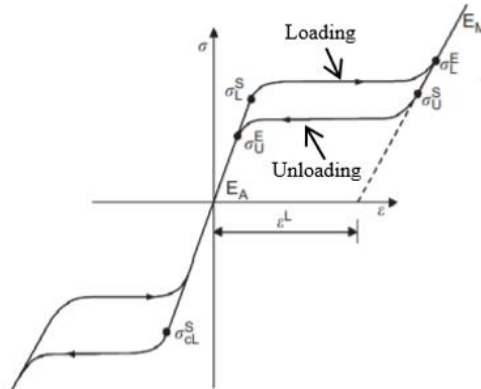


Figure 23 – Superelastic behavior of Nitinol (UMAT Abaqus routine) [62].

The use of this material model requires the specification of 14 material constants on the data lines, which are taken from literature [52] [53] (Table 2).

Table 2 – Nitinol material parameters

| | | |
|----------------|---|---------------------|
| E_A | Young's modulus of austenite (MPa) | 63000 |
| ν_A | Austenite Poisson's ratio | 0.3 |
| Density | (kg/m ³) | $6.5 \cdot 10^3$ |
| | (t/mm ³) | $6.5 \cdot 10^{-9}$ |
| E_M | Young's modulus of martensite (MPa) | 63000 |
| ν_M | Martensite Poisson's ratio | 0.3 |
| ϵ^L | Uniaxial transformation strain | 0.0325 |
| σ_L^S | Stress at which the transformation begins during loading in tension (MPa) | 420 |
| σ_L^E | Stress at which the transformation ends during loading in tension (MPa) | 500 |

| | | |
|-----------------|--|-----|
| σ_U^S | Stress at which the reverse transformation begins during unloading in tension (MPa) | 360 |
| σ_U^E | Stress at which the reverse transformation ends during unloading in tension (MPa) | 280 |
| σ_{cL}^S | Stress at which the transformation begins during loading in compression, as a positive value (MPa) | 495 |
| T_0 | Reference temperature (°C) | 37 |

4.3 FE Simulation

Software used in this study for the FE modelling:

- Pre-processing: *Hypermesh v.2021* (Altair Engineering, Inc., USA)
- Solver: *Abaqus Standard* (Dassault Systemes Simulia Corp., Providence, RI, USA)
- Post-processing: *Hyperview v.2021* (Altair Engineering, Inc., USA)

The FE simulations were run on workstation equipped with Intel Core i7 series 9, 64 bit, 32 GB RAM, Windows 10 Pro.

The simulations were performed as static analyses based on the theory of large displacements, stabilizing the simulation using an artificial damping, upon a constant temperature of 37 °C.

4.3.1 Verification Tests

At first, an uniaxial simulation was performed to check the ability of the constitutive model to correctly reproduce the superelastic effect. A three-dimensional sample with a thickness and width of 5 mm and a length of 40 mm was simulated. Quadratic hexahedral elements C3D8R – 8 node linear brick with reduced integration (see Abaqus Documentation, Elements Guide) were used to realize the mesh. The total number of elements was 8000 and the material parameters are those reported in *Table 2*. One extremity of the sample was fixed (blocking the degrees of freedom in translation and rotation of the nodes) and a tensile displacement of 5 mm was applied on the opposing side. The sample is subjected to a tensile loading-unloading upon a constant temperature of 37 °C. The schematic simulation model is showed in *Figure 24*.

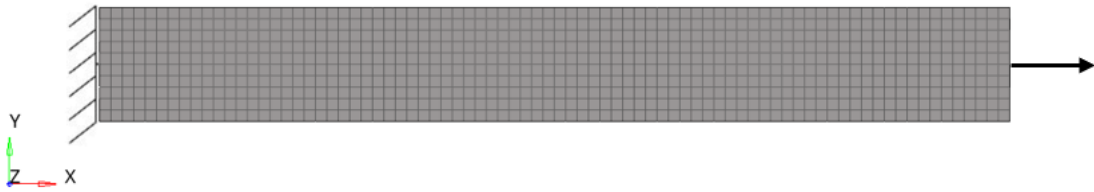


Figure 24 – Three-dimensional beam mesh for tensile test.

4.3.1.1 Staple Opening Simulation

A simple simulation was performed to study the behavior of the staple subjected to an uniaxial load in order to reproduce the opening of the device and evaluate the developed forces. The FE model and material parameters are those described in *chapter 4.2*. The staple was constrained in the middle of the bridge, blocking the 6 degrees of freedom of the corresponding node set. The following conditions were applied to simulate the opening (see *Figure 25*):

- Displacement of 4 mm along transverse axis (x axis) on the extremity of the legs at a distance of 19 mm from the neutral axis of the bridge.
- Displacement of 1.1 mm along transverse axis (x axis) applied on leg profile at a distance of 4 mm from the neutral axis of the bridge.

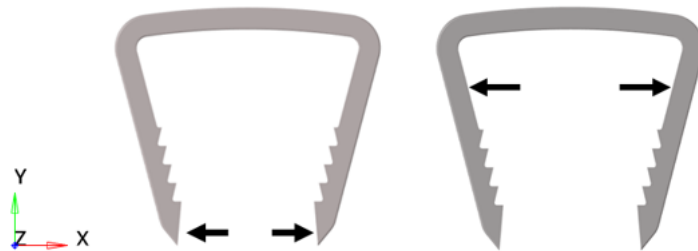


Figure 25 – Schematic view of the two loading conditions.

The displacement was applied using rigids element RBE2, which constitutes a rigid connection that allows to transfer the displacements from an independent node to one or more dependent nodes

Single simulations were composed of two steps. In the first step, axial displacement was assigned to the nodes of the leg. In the second step the displacement was removed and the staple retrieves its original shape (see *Figure 26*). The temperature field was set to 37 °C for all nodes in the simulations.

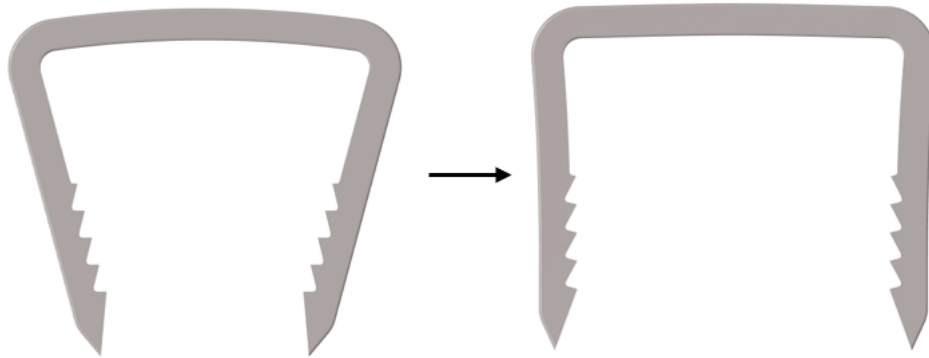


Figure 26 – Generic view of simulation step of staple opening.

4.3.2 Four-point bending standard test simulations

As described in *Chapter 2*, the loading apparatus reported in the ASTM regulation is composed by:

- the testing machine, equipped with a four-points bending fixture device;
- the gripping devices, consisted of a pair of staple extensions that permit the holding of individual staples for the application of bending loads.

A FE model that simulates the experimental four-points bending procedure was implemented. The numerical framework is composed of three components: the staple model, the staple extension frame and the support and loading rollers geometry. The

staple component and nitinol material parameters were the same of the previous simulations, described in *chapter 4.2*. Staple extensions are modelled as steel blocks, of (5 x 20 x 40) mm. Steel material was implemented as elastic isotropic material, with a Young's modulus of 200 000 MPa and a Poisson's ratio of 0.3. To simulate the leg fixation into the hole it was shaped a node-to-node contact interface between staple and staple extension, copying and duplicating the shell mesh of staple leg on the extension block component. This strategy was adopted to prevent mesh convergence problems due to the modelling of contact between two surfaces and reduce the computational time of the final numerical simulation. One staple extension block was composed of 58900 tetrahedral elements (C3D4). At last, the support rollers were meshed with SFM3D4R 4-node quadrilateral surface element with reduced integration (see Abaqus Documentation, Elements Guide). Each one was 6 mm long with a radius of 2 mm and is composed of 930 elements with an element size of 0.40 mm. The horizontal distance between the upper and its adjacent lower rollers' center was set to 16 mm.

The roller and staple extension interactions and connections were implemented with a hard surface to surface contact, by using the contact-pair algorithm (defining master and slave surface), with a friction coefficients equal to 0.10 (steel on steel interaction) [63]. Due to the model's axial symmetry, only half of the model was simulated and symmetrical boundary conditions were applied along the cross-section in the middle of the staple bridge. Each boundary condition was applied to a nodes set. A displacement of 3.0 mm in the longitudinal direction (y axis) was applied to the nodes of the upper roller to simulate the loading state while nodes of the lower roller were constrained blocking all degrees of freedom. The simulation was stabilized by setting an

adequate damping factor and a minimum time increment allowed for the step. The temperature field was set equal to 37 °C for all nodes.

Thereafter, two different device insertion configurations were simulated, with the aim of verifying the consistency of the results obtained by the adopted model. Initial and final deformed geometries at the end of the simulations conducted are reported in summary in *Figure 27*.

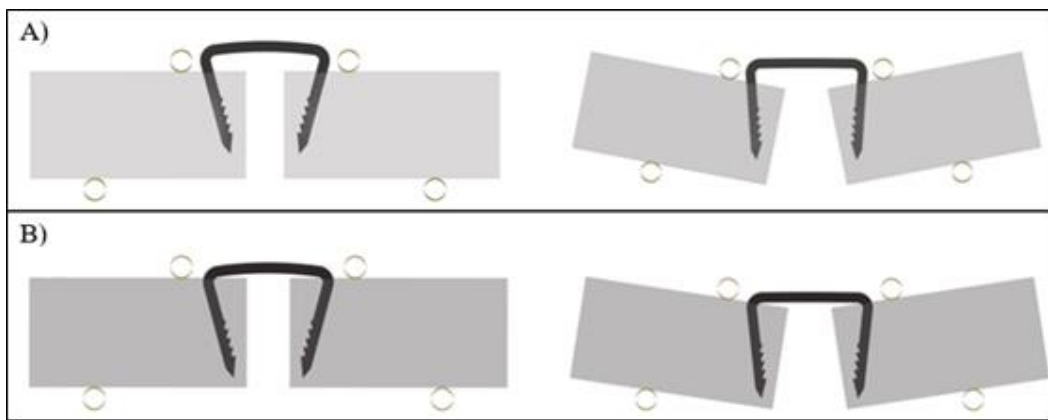


Figure 27 – *ASTM Preliminary Tests. A) Staple in standard configuration with an insertion gap of 2 mm. B) Staple in standard configuration completely inserted.*

Subsequently, the following modifications were carried out to simulate a set up more similar to an experimental one:

- Taking into account the paper [64] cited in the ASTM regulation that examined the bending rigidity of bone stainless steel staple, set up dimensions were increased.
- Friction coefficient between extension blocks and rollers was set to zero (simulating a free frictionless rotation of the actuator).

Keeping the same boundary conditions and mesh type as the previous simulations, the bending test was performed in a four-points bending apparatus of bigger dimensions.

These final simulations were done in order to optimize the configuration of the test setup and to evaluate the dependence of the applied load as a function of the size of the loading machine, while maintaining the same bending moment effect. A second step was also implemented that simulated the return in an unloading condition.

Three simulations were carried out (see *Figure 28*), in detail:

- Staple in standard “closed” configuration with an insertion gap of 2 mm.
- Staple in standard “closed” configuration with a complete insertion.
- Staple with an angle-leg of 90° with a complete insertion.

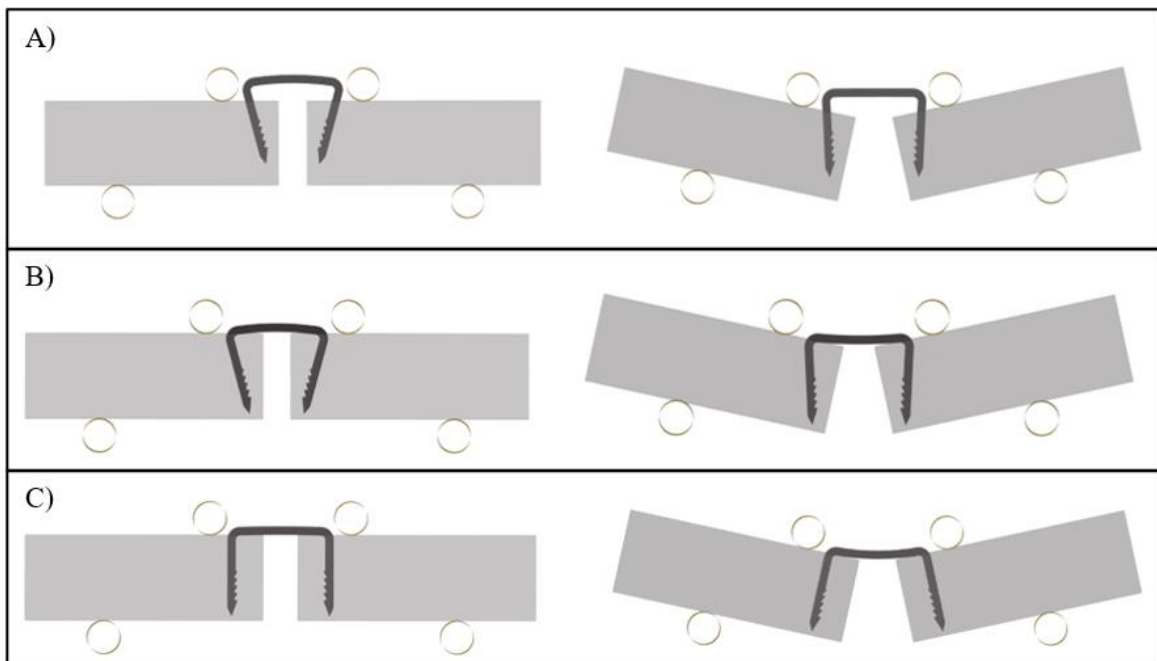


Figure 28 – ASTM Final Tests. A) Staple in standard configuration with an insertion gap of 2 mm. B) Staple in standard configuration completely inserted. C) Staple in open configuration completely inserted.

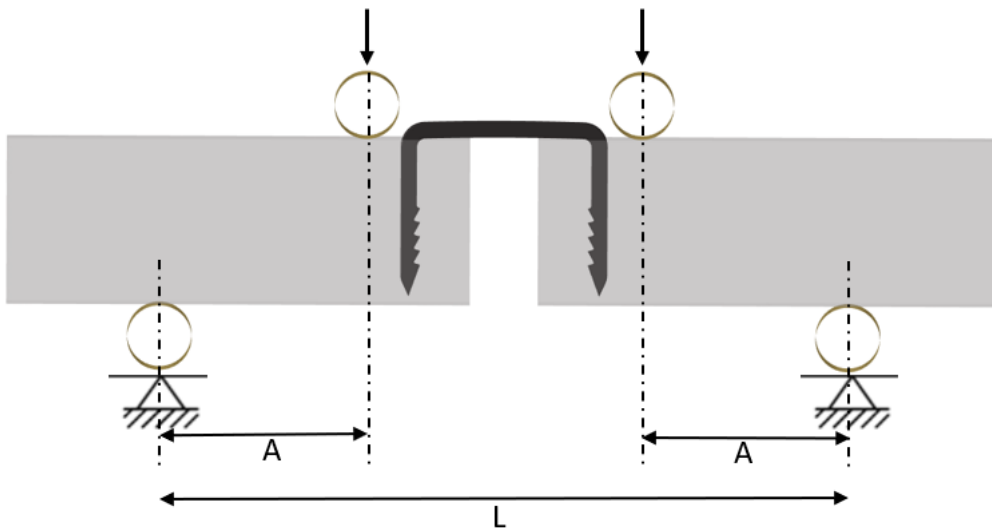


Figure 29 – Staple in Four-Point Bending Load Apparatus Scheme of Numerical Simulation.

Figure 29 shows in detail the geometry of the setup used for the last simulations mentioned. All simulations were performed with the following parameters:

- $A = 25\text{mm}$
- $L = 80\text{ mm}$
- Roller Diameter = 8 mm
- Staple Extension Block Size = (56 x 20 x 10) mm
- Displacement = 5 mm
- Simulation time: 1s
- CF roller-block: 0 → surface to surface contact
- Staple-Block → node to node contact

Boundary conditions adopted are following reported in summary.

- Symmetry constraint:

$$U_x = 0$$

$$Rot_y = 0$$

$$Rot_z = 0$$

- Axial constraints, to keep the blocks bending in the plane of load:

$$U_z = 0$$

$$Rot_x = 0$$

$$Rot_y = 0$$

- Roller above:

$$U_x = 0, U_y = -5, U_z = 0$$

$$Rot_x, Rot_y, Rot_z = 0$$

- Roller under:

$$U_x, U_y, U_z = 0$$

$$Rot_x, Rot_y, Rot_z = 0$$

The three components have the following characteristics:

- Staple (an half): 104 441 C3D4 tetrahedron elements, 20 851 nodes.
- Staple extension block: 154 957 C3D4 tetrahedron elements, 36 732 nodes.
- Roller: 3416 SFM3D4R 4-node quadrilateral surface elements, 1769 nodes.

4.4 FE Simulations output

The mechanical performance of the bone staples was firstly assessed by considering the forces generated by the applied displacement. Indeed, it is essential that an adequate compression force is developed *in vivo*. This is one of the main factor that influences staple choice and the ability to stabilize the fracture site: it is important to optimise clamping force because excessive strength can provoke pressure necrosis and prevent healing, while insufficient one can slow healing and may even allow fracture recurrence [34]. Moreover, maximum principal stress and maximum principal strain to evaluate the most critical regions.

All results reported in this work were extracted with the aid of MATLAB R2021b (MathWorks, USA), Microsoft Excel, HyperView, and Abaqus CAE (implementing a python script). Using a python script, nodal RFs were extracted and summed together for each timestep of the simulations.

In outline, the biomechanical quantities that were considered to evaluate the staple frame mechanical performance are:

- The reaction force magnitude along the loading axis developed during the loading-unloading cycle, in correspondence with the area of the forces application.
- The displacement along the loading plane.
- The percentage of opening: ratio between each sub-step displacement and the one corresponding with a complete staple opening.
- The deflection angle: angle between the horizontal axis and the inclined plane of the staple extension block under bending loading.

- The peak value of maximum principal stress and the peak value of maximum principal strain to verify the superelastic staple behaviour and to evaluate the most critical region of the device.
- The contact normal forces (CNORMF) were extracted between the support roller and the staple extension block to evaluate the load magnitude during the simulation step.

5 RESULTS

5.1 Uniaxial Tensile Test

The numerical simulation of the uniaxial tensile strength shows that the sample developed a recoverable deformation of about 4%, as shown in the stress-strain response in *Figure 30*. Indeed, when the stress is removed, the sample completely recovered its original shape configuration. Values obtained of stress maximum principal and strain maximum principal are reasonable compared to the results of mechanical testing and other works [51][65] [66].

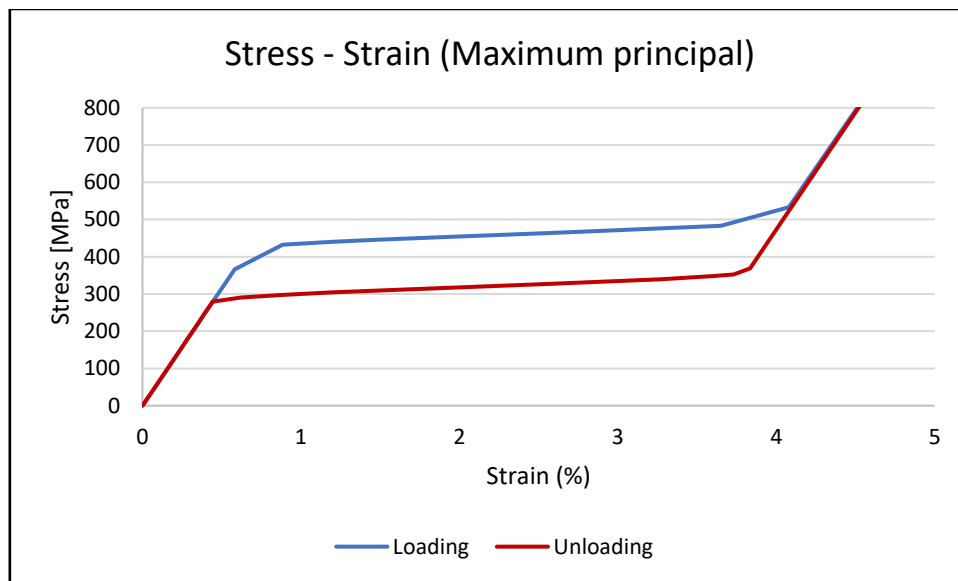
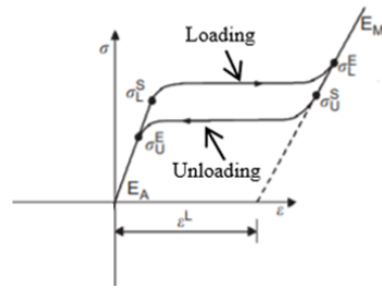
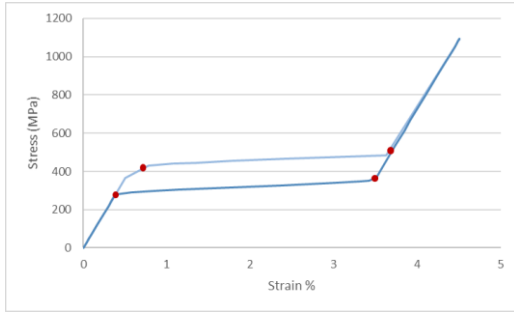


Figure 30 – Stress vs Strain response for uniaxial tensile stress showing the superelastic effect of the material.

Furthermore, the obtained stress and strain peak values agreed well with the material parameters selected for the model (see *Figure 31*).



- $\sigma_L^S = 420 \text{ MPa}$
- $\sigma_L^E = 500 \text{ MPa}$
- $\sigma_U^S = 360 \text{ MPa}$
- $\sigma_U^E = 280 \text{ MPa}$
- $\epsilon^L = 3.25 \%$

Figure 31 – Superelastic behaviour of Nitinol (with a focus on model parameters chosen). On the left the stress-strain curve obtained from the uniaxial tension test. On the right the theoretical stress-strain curve with the reported material's parameter chosen.

5.2 Staple opening

The staple opening behaviour was analysed with the following parameters: absolute maximum principal stress, absolute maximum principal strain, reaction force and bending moment. Results for the two loading configurations are reported in *Figure 32*.

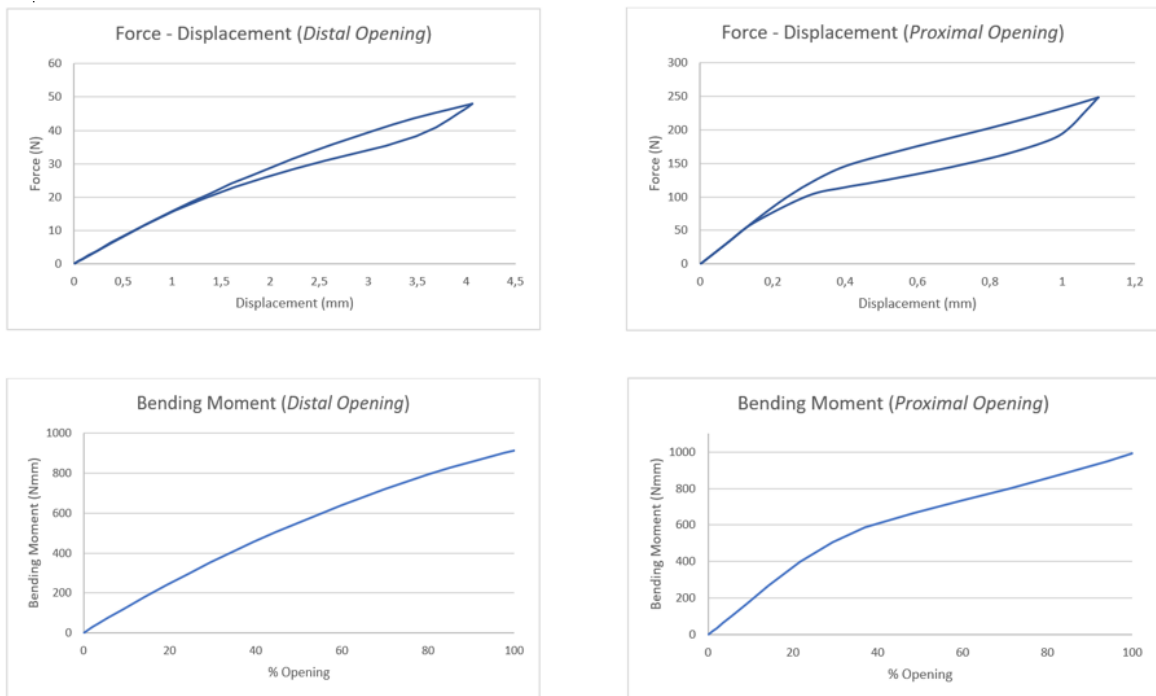


Figure 32 – Curves of Reaction Force developed for each leg versus the displacement and Bending Moment comparison.

In the case of a distal opening, the maximum force developed along the loading axis (x axis in this case) is 48 N, corresponding to the state of complete opening. On the other side, in a proximal opening the maximum force corresponding to a complete opening is about 248 N. Instead, the values of the bending moments respect to the neutral axis of the bridge are perfectly comparable, with a maximum deviation of about 8.06%. Maximum principal stress contour plots were analysed in order to evaluate the most critical region for the integrity of the structure in the two different loading conditions. Even stress-strain curves of the element most stressed were reported in *Figure 33*, which shows the hysteresis loop of the material.

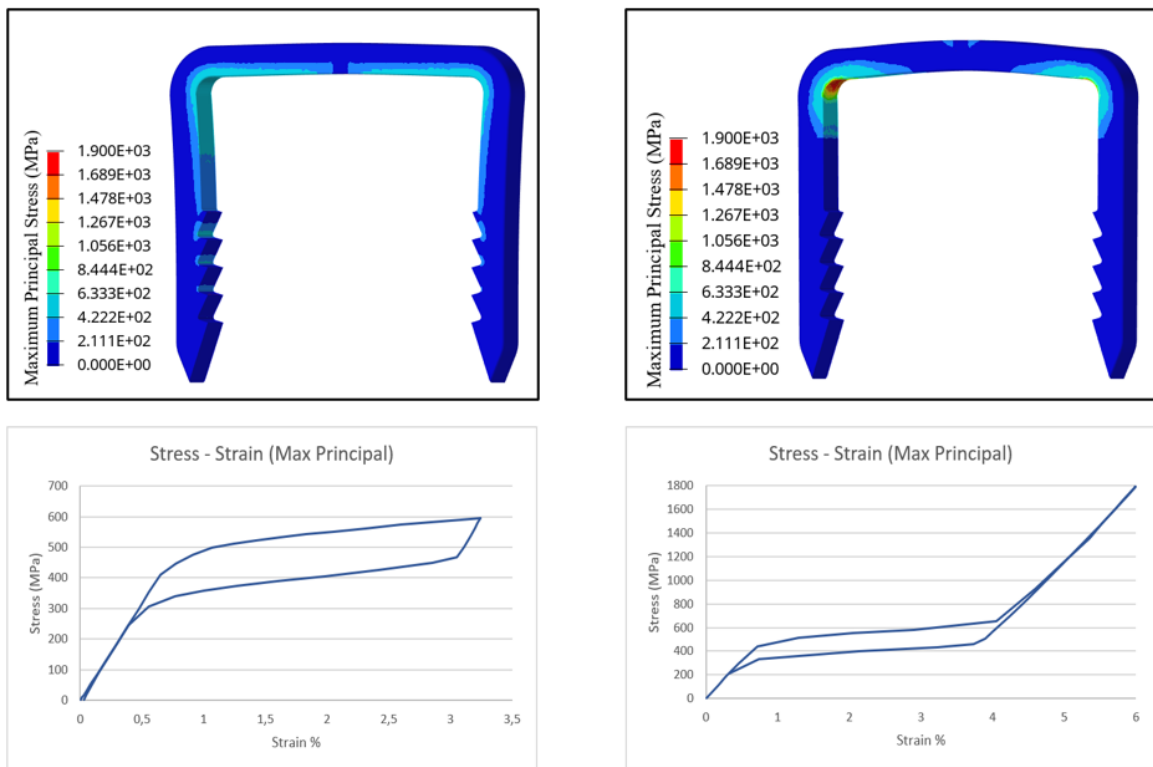


Figure 33 – Maximum Principal Stress contour plots and relative stress-strain curve for the two configurations of staple opening.

5.3 Results of four-point bending tests

The first model implemented for simulating the four-points bending test was evaluated in two different configurations, changing staple insertion condition. Force developed by the loading apparatus versus the actuator deflection was first compute, afterwards bending moment versus the deflection angle was estimate as reported in the regulation (see *Chapter 2.2*).

Figure 34 reports the curves of applied force and bending moment for each of the two simulated configurations for the loading step. Since only half a device was considered, the force was calculated by multiplying the simulation values by two.

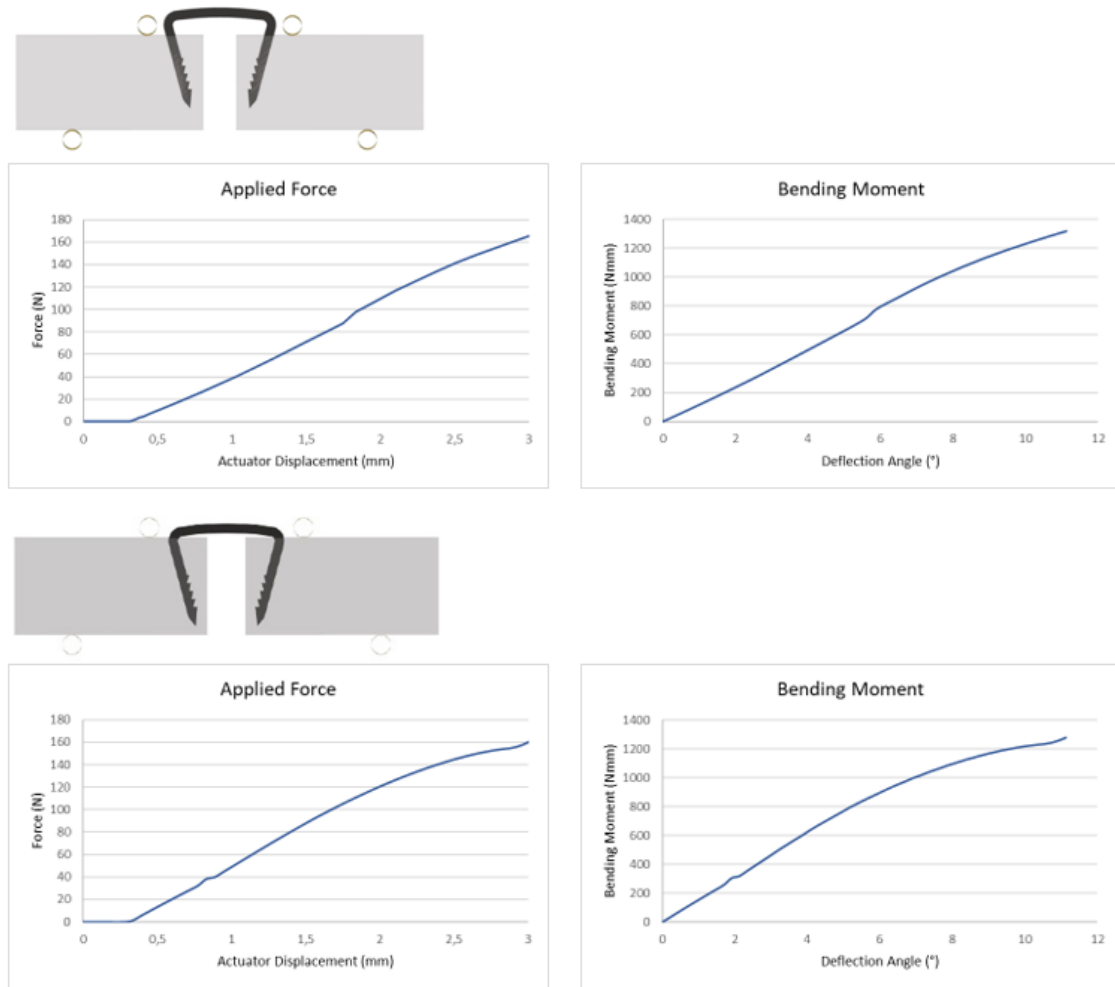


Figure 34 – Results of Applied Force and Bending Moment for the two configurations.

Another assessment was conducted, plotting the maximum principal stress and maximum principal strain. Indeed, stress and strain histories are of particular value in estimating the frame's structural integrity and damage risk during a bending loading.

Figure 35 reports the contour plots of stress and strain of the configuration in which the staple is completely inserted into the extension blocks. Under the same load conditions, this is the case where higher stresses develop in the site of implant.

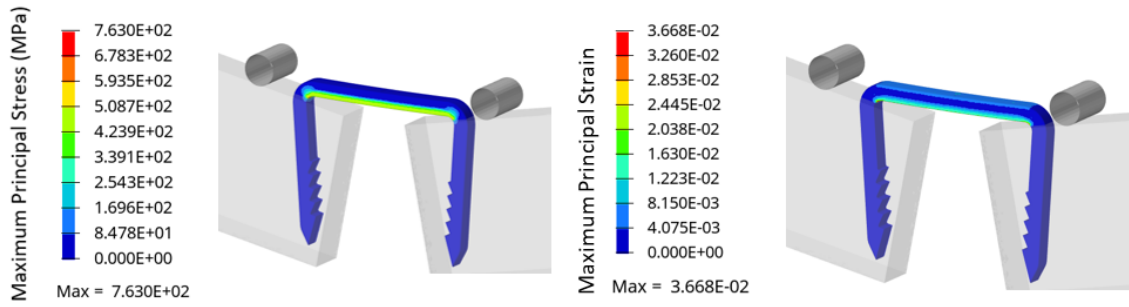


Figure 35 – Contour Plots of the last geometry: Maximum Principal Stress on the left and Maximum Principal Strain on the right.

Additionally, to compare these results the stress-strain curve of the loading phase is reported in *Figure 36* for the two configurations. The diagram represents the values of maximum principal stress and maximum principal strain of the highest stressed element.

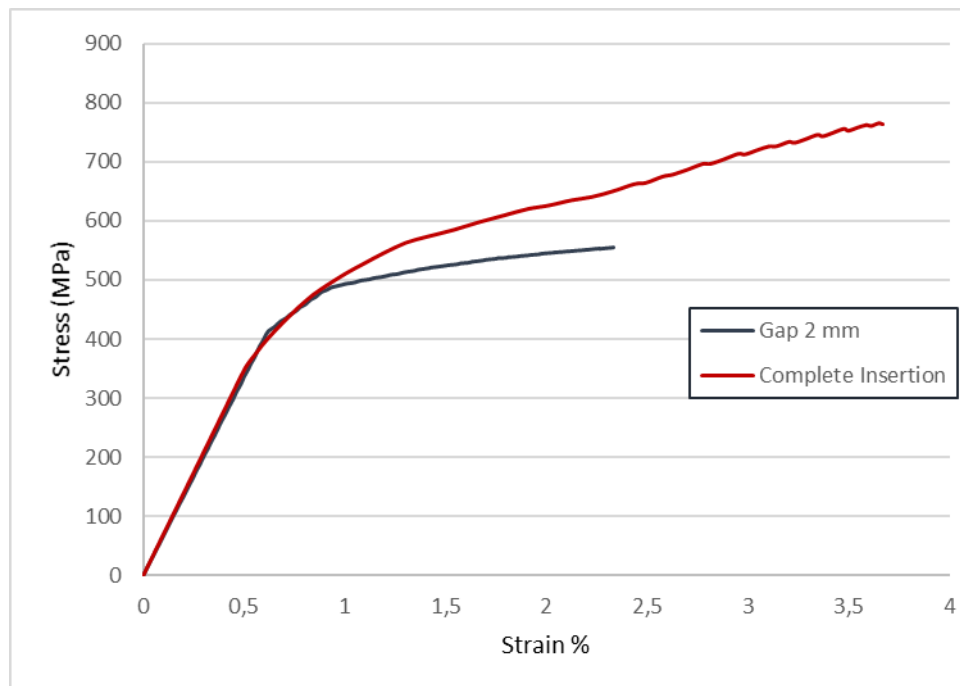


Figure 36 – Maximum Principal Stress and Strain curves for the highest stressed element for the two set up configurations.

Given all the previously reported results, two different modifications aiming to enhance outcomes compared to experimental setup were pursued: frame model modifications (bigger dimensions of rollers and staple extension blocks) and friction coefficient between rollers and blocks set to zero.

As described in *Chapter 4.3.2*, in this case three different staple insertion configurations are investigated, to analyse the entities of the force in different insertion configuration and with a changing in staple design. Force developed by the loading apparatus versus the actuator deflection was first compute, afterwards bending moment versus the deflection angle was estimate as reported in the regulation (see *Chapter 2.2*). *Figure 37* reports the curves of applied force and bending moment for each of the three simulated configurations for the loading and unloading steps. Since only half a device was considered, the force was calculated by multiplying the simulation values by two.

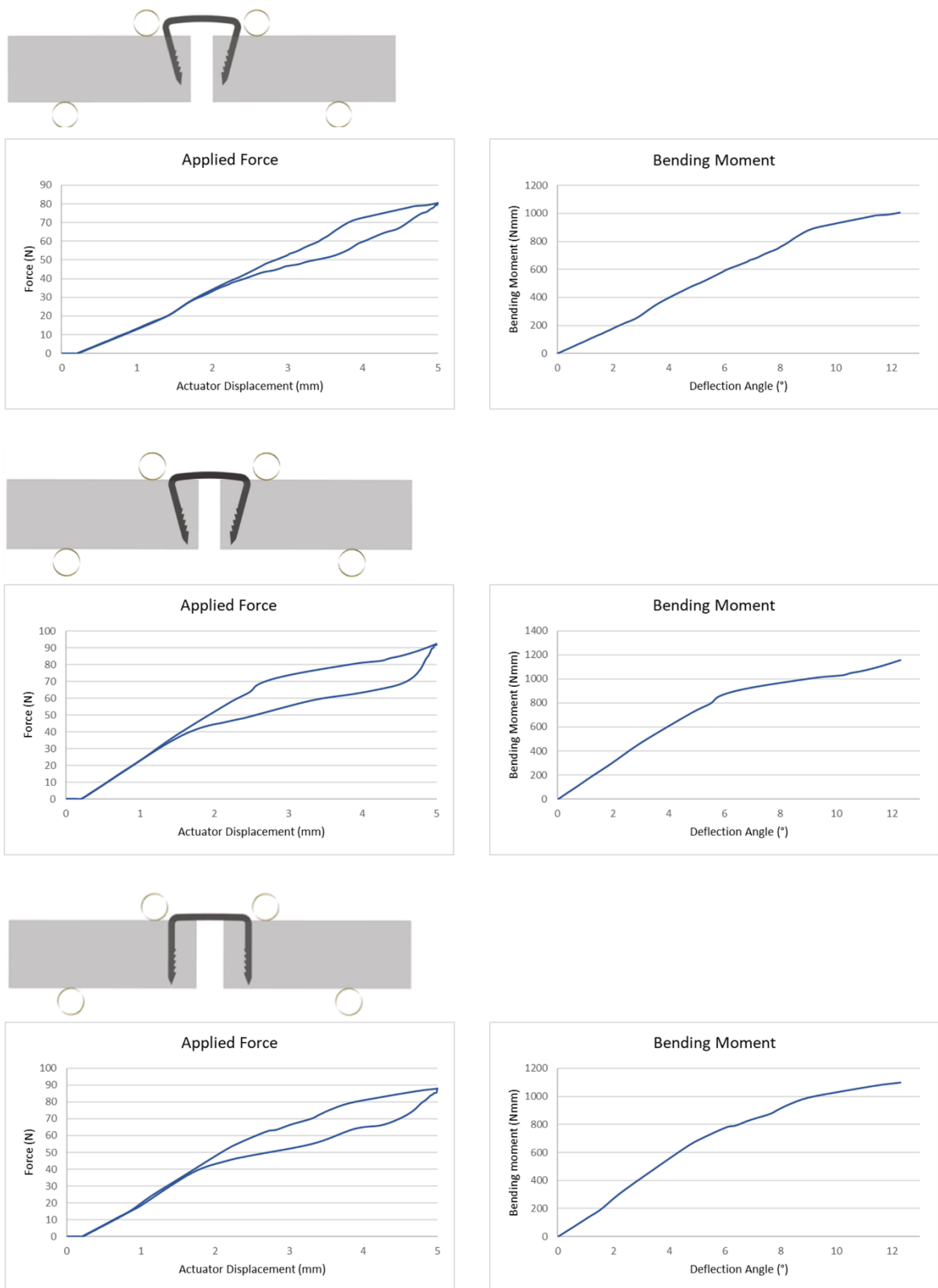


Figure 37 – Results of Applied Force and Bending Moment for the three configurations.

Compared to the preliminary tests, with this numerical framework, smaller forces are developed for the same displacement of the actuator. If we take as an example the first configuration in which the staple is in standard configuration and has an insertion gap of 2 mm, for a displacement of 3 mm a force of about 160 N develops in the first case while, in the final set up, a force of about 80 N. On the other hand, the values of bending moments appear comparable with the same angle of deflection for both geometries.

Additionally, *Figure 38* reports the hysteric behavior plotting the maximum principal stress and strain of the most stressed element of the staple.

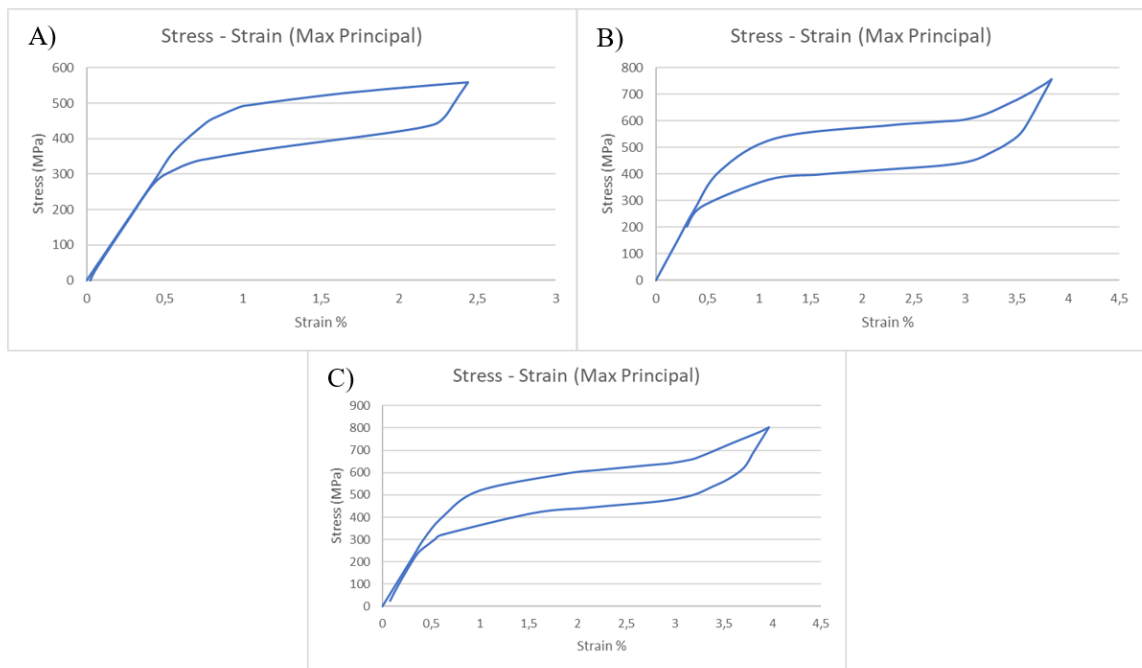


Figure 38 – Max. Principal Stress and Strain of the highest stressed element. A) Staple in standard configuration with a 2 mm of insertion gap. B) Staple in standard configuration with complete insertion. C) Staple in open configuration with complete insertion.

The plots of the hysteresis cycle show that, when the device is completely inserted inside the extension blocks, stress and strains of greater value are developed.

5.4 Fatigue analysis

Because the device is subjected to cyclic loading during use, it is of particular interest to evaluate the fatigue behavior of the material. As reported in the FDA Guidance “*Technical Considerations for Non-Clinical Assessment of Medical Devices Containing Nitinol*” [67] computational analyses are useful to calculate fatigue safety factor(s) using a constant life curve. Indeed, unlike traditional metals, which utilize stress-based fatigue life estimates (e.g., Goodman, Soderberg diagrams), using a constant life mean versus alternating strain diagram has been found to provide a good model for fatigue life prediction for nitinol [68].

Analyses were conducted considering the cyclic fatigue and durability properties of Nitinol-based endovascular stents literature [69]. Within this work *strain-based constant-life diagram* for SMA’s materials was used to assess the fatigue durability of the device. In detail, the strain-based constant-life approach is an uniaxial diagram reporting the strain amplitude ε_a and the mean strain ε_m at a fixed number of cycles N (e.g. 10^7) [70].

Firstly, ε_a and ε_m were computed for the staple in complete insertion, which is the case where greater strain develop under the same loading conditions. These parameters were computed as mean and alternating first principal strains, respectively ε_a and ε_m , that occur in each point of the structure. Strain values were calculated using the following definitions reported by Scalet and colleagues [70]:

$$\varepsilon_m = \frac{\varepsilon_{(i)} + \varepsilon_{(i+1)}}{2}$$
$$\varepsilon_a = \left| \frac{\varepsilon_{(i)} - \varepsilon_{(i+1)}}{2} \right|$$

where subscripts $i+1$ and i denotes, respectively, the last sub-step of a generic load step and the last sub-step of the following unload step.

In this work, one loading cycle consist of applying a bending load starting from a resting condition, reach the maximum strain peak, then unloading until the rest state. Indeed, herein the strain of the last sub-step of the unload step is zero, which results in a value of zero of the parameter R ($\epsilon_{\min}/\epsilon_{\max}$).

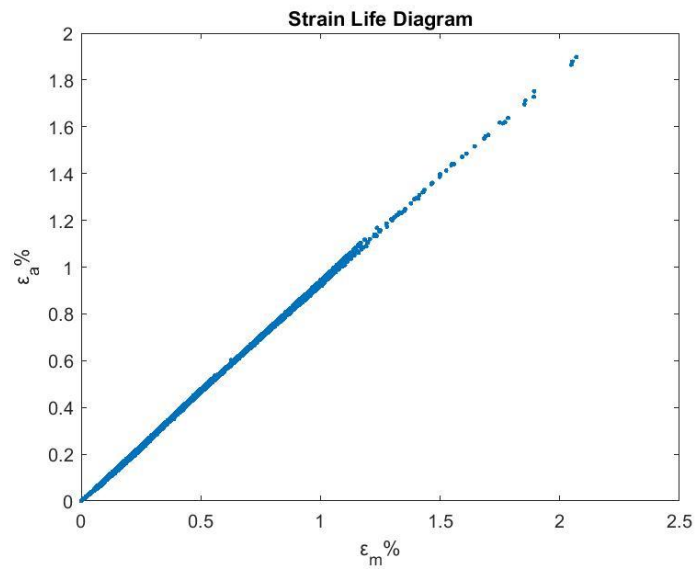


Figure 39 – Numerical results obtained for the strain constant life diagram.

Figure 39 reports the numerical results obtained for the Strain-Based Constant Life Diagram.

6 DISCUSSION

6.1 Preliminary Tests

A comparison with the FE literature was conducted to verify the predictive capability of the model. *Table 3* summarizes the clamping force developed in previous FE studies on Nitinol staple. For all the works into consideration, the maximum value of clamping force was computed in the distal part of the legs of the staple. This is the zone of the device where peak of force are concentrated during staple-bone contact. *Table 3* reports force values that are comparable with that found in the first simulation (distal opening) in *Figure 32*. It should be considered that variations in the magnitude of the developed forces are also due to different designs of the staple. For example, in the study of Subasi et al. [53] a staple 43.4% thicker than the device treated in this thesis, developed a clamping force of about 245 N.

Table 3 – Comparison with literature FEA studies.

| | | |
|---|--|---|
| Omer Subasi , Shams Torabnia , Ismail Lazoglu [53] | F = 70.2 N (wire geometry staple) F = 245 N (rectangular geometry staple) | NOTE Staples optimized for Sternal loading model |
| Daniel Christ, Stefanie Reese [54] | F = 36 N | |
| Krone et al. [55] | F = 33 N | NOTE Numerical test supported by <i>in vivo</i> mechanical test |

| | | |
|--|-------------------|--|
| A.F. Saleeb n, B. Dhakal, J.S. Owusu-Danquah [52] | F = 56.6 N | |
|--|-------------------|--|

Force versus displacement curves clearly show the non-linear behaviour of nitinol material, highlighting the hysteresis loop of the loading cycle. Additionally, further investigation about Maximum Principal Stress and Strain can be used to predict the structural integrity of the device and evaluate critical regions.

In silico preliminary tests of ASTM regulation are useful to calibrate the geometry of the loading apparatus, evaluate computational time estimate the value of displacement to be imposed in the test. These preliminary simulations show that the insertion gap is a parameter that will have to be taken into account during experimental tests. Under the same boundary conditions, when the staple is fully inserted into the extension block higher values of stress and strain are developed.

6.2 Four-Points Bending Tests

The numerical framework implemented for the standard tests allows to obtain the load-displacement curve required by the regulation. One parameter that influences the entity of the load to be applied is the dimension of the loading apparatus, especially the diameter of the roller, the size of the staple extension block, and the distance between loading and support roller that affects the final bending moment of the construct. It is also advisable to minimize the friction between the rollers and the blocks as much as possible, in order to have the same final displacement with the use of less force.

6.2.1 Insertion Gap

In this work two configurations were evaluated, with the goal of understanding how much a gap between the underside of the staple bridge and edge of the staple extender could influence the outcomes of the simulations.

As shown in *Figure 37* and *Figure 38*, under the same loading conditions, a staple fully inserted into the blocks is affected by higher stresses in its structure, especially at the insertion site. On the other hand, force magnitude is of the same order for both cases, reaching the peak of 80 N with a 2 mm of gap, and a peak of about 90 N without insertion gap. Additionally, *Figure 40* reports the contour plots of the Von Mises stress of the staple device, showing comparable values for both configurations. Consequently, attention should be paid to the site of insertion.

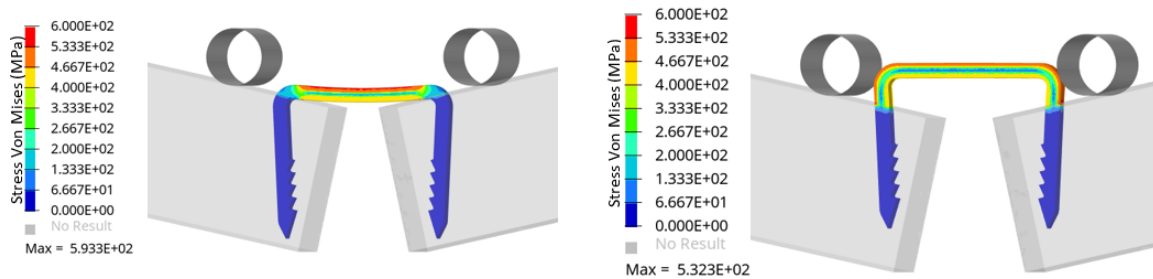


Figure 40 – Contour plots of Von Mises Stress of a complete inserted staple (on the right) and a gap of 2 mm (on the left).

6.2.2 Device Design: Angle – Leg

Another assessment was performed to evaluate the incidence of the angle between leg and bridge of the staple. Two geometries with different angles were analysed: one with an angle of 90° and one with an angle of 75°. Force versus displacement curves report the same value of about 90 N for an actuator displacement of 5 mm. The last two

diagrams of *Figure 38* report these following values of maximum principal stress and maximum principal strain:

- *Standard Staple* (angle leg 75°): $\sigma_{MAX} = 755.82$ MPa, $\epsilon_{MAX} = 3.84\%$
- Staple with angle-leg of 90° ; $\sigma_{MAX} = 802.35$ MPa, $\epsilon_{MAX} = 3.97\%$

This simulation is an example of how the framework implemented is also useful for comparing the mechanical performances of different devices.

6.2.3 Stiffness Estimation

Once the load-displacement curve was obtained, it is possible to estimate the stiffness of the construct. In accordance with the regulation, the stiffness of the construct could be calculated by measuring the initial slope of the load-displacement curve, where there is an initial elastic behaviour. The bending stiffness values are comparable with experimental studies. R. McKnight et al. [71] analyse three Nitinol staples subjected to a four-points bending load and computed the value of bending stiffness for each constructs: 39.6 N/mm, 28.1 N/mm and 28.6 N/mm. *Figure 41* shows the case in which the staple is inserted and report an estimate value of stiffness of our construct of about 29 N/mm, that is comparable with others find in literature.

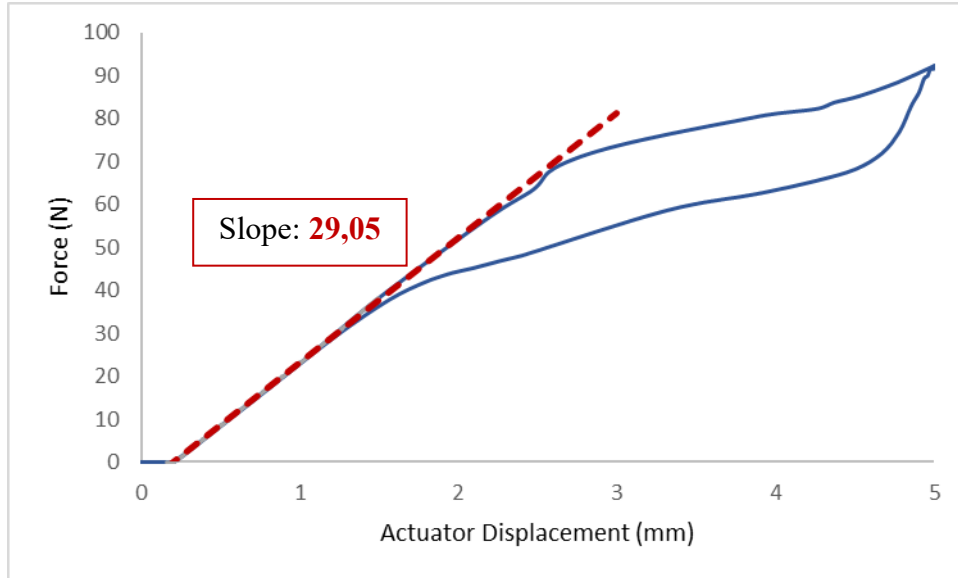


Figure 41 – Force-displacement curve with stiffness estimation.

6.3 Fatigue analysis

Technical standards indicate in vitro tests as a suitable approach for the assessment of staple fatigue behavior. As mentioned in *Chapter 5.4*, FEA is useful in fatigue analysis since the first cycle is considered to provide the worst case stress-strain conditions [69]. There are several fatigue criteria that could be used in numerical analysis of fatigue behaviour. In this thesis has been implemented the scalar method, based on mean and amplitude first principal strains [70], considering uniaxial loading cycling between zero and a given strain. However, for more complex three-dimensional states of strain (and stress), there is no guarantee that the criteria compute meaningful values for fatigue predictions. The most efficient way to get a more thorough understanding of NiTi mechanical behaviour is to perform an accurate experimental campaign of material characterization on specimens, designed according to the proper shape and dimensional constraints [72][73].

Figure 39 reports the numerical results obtained in this study for the Strain Constant Life Diagram. Because the minimum strain is zero, the computed points of the structure are arranged along a straight line. It can be expected that, under this loading condition used for a static analysis, the specimen will be fail under fatigue tests.

For validating this method, material parameters provided by the manufacturer are necessary and experimental data that supply the experimental limit curve referred to N cycles. Indeed, for validating the approach, a larger number of different loading conditions and designs should be considered.

6.4 Limits of the proposed model

This study presents some limitations. Simulation outputs depend on the material parameters, type of staple, dimension and contact modeling of the frame of the loading apparatus described in the regulation. The effects of Nitinol material plastic deformation and inelastic strains were not considered. Moreover, these are preliminary numerical test, in which force developed during preloading (opening) of the staple before implantation is not considered.

Subsequently, it is necessary to proceed with the validation with experimental tests of the model to determine if this accurately represents the experimental results. To perform this task, it is necessary to carry out mechanical tests in the laboratory, obtain material parameters from the manufacturer and optimize *in silico* tests with the same characteristics and boundary conditions as *in vivo* tests.

7 CONCLUSION AND FUTURE DEVELOPMENTS

Considering the FE models presented within this thesis work, some conclusions could be evaluated. At first, simulation outcomes will have to be compared with experimental results, to validate the proposed model. Indeed, once the FE model is calibrated, numerical analyses can be used to evaluate the structural integrity of the device and predict future behavior avoiding time and costs of the experimental tests. Computational simulations can facilitate the design, optimization and development phases of medical devices [74], reducing the number of prototypes to be manufactured and the experimental tests, with positive impact on the product development cycle. *In silico* medicine can radically change the product life phases of medical devices. It can reduce the cost associated with the experimentation of the devices and their regulations, optimize the design, improve security and effectiveness, and reduce costs and time of the production phases [75].

The work presented is a preliminary study. It is necessary to carry out experimental mechanical tests so that they have the same characteristics as the *in silico* tests, and subsequently calibrate the FE model, to reproduce the laboratory tests as faithfully as possible. Regarding the fatigue tests, the proposed methodology represents a promising engineering tool for the evaluation of Nitinol fatigue life; future work should be focused on its validation relying on appropriate experimental fatigue data and its application to other designs, implant configurations, loading and boundary conditions.

The DynaNite staple (Arthrex) was bought by Intrauma S.p.A. company and the geometry was recreated scanning the device. Future steps include implementing the scanned geometry in the framework herein proposed. Thereafter an experimental

campaign will be conducted and results of the experimental tests will be compared with numerical results, for the FE model validation. The implemented framework is flexible enough to apply to other devices. Next step is to make the framework easily modifiable for different device geometries.

In conclusion, *in silico* standard testing is currently an evolving technology. In this study it emerges the potential of computational modelling in efficiently supporting the characterization phases of staple devices. FE modelling allows to both analyse mechanical outcomes of the device, and reduce times and costs associated to the iterative device research and development cycle.

REFERENCES

- [1] J. Walker, “Skeletal system 1: the anatomy and physiology of bones,” *Nurs. Times [online]*, vol. 116, no. 2, pp. 38–42, 2020.
- [2] G. D. Heaney, Robert Proulx and Whedon, ““Bone,”” *Encyclopedia Britannica*, 2019.
- [3] G. Li and W. Niu, *Challenges toward musculoskeletal injuries and diseases*. 2020.
- [4] B. C. Bartl R, “Structure and architecture of bone,” in *Bone Disorder: Biology, Diagnosis, Prevention, Therapy*, 2017.
- [5] D. J. Hadjidakis and I. I. Androulakis, “Bone Remodeling,” *Ann N Y Acad Sci*, vol. 396, pp. 385–396, 2006, doi: 10.1196/annals.1365.035.
- [6] D. W. Dempster, “Osteoporosis and the Burden of Osteoporosis-Related Fractures,” *Am. J. Manag. Care*, vol. 17.6: S164, 2011.
- [7] M. Gass and B. Dawson-hughes, “Preventing Osteoporosis-Related Fractures : An Overview,” *Am. J. Med.*, vol. 119, pp. 3–11, 2006, doi: 10.1016/j.amjmed.2005.12.017.
- [8] F. Borgström *et al.*, “Fragility fractures in Europe: burden, management and opportunities,” *Archives of Osteoporosis*, vol. 15, no. 1. 2020, doi: 10.1007/s11657-020-0706-y.
- [9] T. A. Einhorn and L. C. Gerstenfeld, “Fracture healing : mechanisms and interventions,” *Nat. Publ. Gr.*, pp. 1–10, 2014, doi: 10.1038/nrrheum.2014.164.
- [10] C. S. Bahney *et al.*, “Cellular Biology of Fracture Healing,” *Regen. Med. Orthop.*, no. January, 2019, doi: 10.1002/jor.24170.
- [11] Office of the Surgeon General (US), “Bone Health and Osteoporosis: A Report of the Surgeon General,” 2004.
- [12] M. Bottlang *et al.*, “Biomechanical concepts for fracture fixation,” *J. Orthop. Trauma*, vol. 29, no. 12, pp. S28–S33, 2015, doi: 10.1097/BOT.0000000000000467.
- [13] A. Merolli and P. T. Leali, *Using bone repair materials in orthopaedic surgery*,

- no. 2. Woodhead Publishing Limited, 2009.
- [14] M. S. Taljanovic, M. D. Jones, J. T. Ruth, J. B. Benjamin, J. E. Sheppard, and T. B. Hunter, "Fracture Fixation," *Radiographics*, vol. 23, no. 6, pp. 1569–1590, 2003, doi: 10.1148/rg.236035159.
- [15] C. N. Cornell, "Internal Fracture Fixation in Patients With Osteoporosis," *J. Am. Acad. Orthop. Surg.*, vol. 11, no. 2, pp. 109–119, 2003.
- [16] R. Ben-ad, "Fixation Updates for Hallux Valgus Correction," *Clin. Podiatr. Med. Surg.*, vol. 31, pp. 265–279, 2014, doi: 10.1016/j.cpm.2013.12.008.
- [17] R. M. Harrington, K. M. Lee, P. A. Anderson, A. F. Tencer, and D. Kowalski, "Factors Affecting the Pullout Strength of Cancellous Bone Screws," *J Biomech Eng*, vol. 1, no. August 1996, pp. 1–8, 1996.
- [18] J. Okazaki, Y., Hayakawa, E., Tanahashi, K., & Mori, "Mechanical Performance of Metallic Bone Screws Evaluated Using Bone Models," *Model. Mater.*, vol. 13(21), 2020.
- [19] ASTM F543 – 17, "Standard Specification and Test Methods for Metallic Medical Bone Screws." .
- [20] K. M. Franssen BB, Schuurman AH, Van der Molen AM, "One century of Kirschner wires and Kirschner wire insertion techniques: a historical review," *Acta Orthop Belg.*, vol. 76(1), pp. 1–6, 2010.
- [21] T. C. Mereau, Trinity M.; Ford, "Nitinol Compression Staples for Bone Fixation in Foot Surgery," *J. Am. Podiatr. Med. Assoc.*, vol. 96, no. 2, pp. 102–106, 2006.
- [22] M. D. Bargar WL, Sharkey NA, Paul HA, "Efficacy of bone staples for fixation," *J Orthop Trauma*, vol. 1(4), pp. 326–30, 1987.
- [23] "<https://www.smith-nephew.com/professional/products/all-products/staples/>." .
- [24] U. Rethnam, J. Kuiper, and N. Makwana, "Mechanical characteristics of three staples commonly used in foot surgery," *J. Foot Ankle Res.*, vol. 2, no. 1, pp. 1–5, 2009, doi: 10.1186/1757-1146-2-5.
- [25] "<https://a-zortho.com/>." .
- [26] F. F. Firoozbakhsh, Keikhosrow K.; DeCoster, Thomas A.; Moneim, Moheb S.;

- McGuire, Michael S.; Naraghi, “Staple leg profile influence on pullout strength: a biomechanical study,” *Clin Orthop Relat Res.*, vol. 331(), pp. 300–307, 1996, doi: 10.1097/00003086-199610000-00042.
- [27] B. P. Bechtold JE, Meidt JD, Varecka TF, “The effect of staple size, orientation, and number on torsional fracture fixation stability,” *Clin Orthop Relat Res.*, vol. 297, pp. 210–7, 1993.
- [28] J. C. Wu, A. Mills, K. D. Grant, and P. J. Wiater, “Fracture Fixation Using Shape-Memory (Nitinol)Staples,” *Orthop. Clin. North Am.*, vol. 50, no. 3, pp. 367–374, 2019, doi: 10.1016/j.ocl.2019.02.002.
- [29] Ryhanen J, *Biocompatibility Evaluation of Nickel-Titanium Shape Memory Metal Alloy [dissertation]*. Department of Surgery, University of Oulu, Oulu, Finland, 1999.
- [30] H. P. Y. P J Yang, Y F Zhang, M Z Ge, T D Cai, J C Tao, “Internal fixation with Ni-Ti shape memory alloy compressive staples in orthopedic surgery. A review of 51 cases,” *Chin Med J*, vol. 100(9), pp. 712–4, 1987.
- [31] <https://www.medshape.com/products/dynaclip/>, “DYNACLIP BONE FIXATION SYSTEM.” .
- [32] C. Y. Tang RG, Dai KR, “Application of a NiTi staple in the metatarsal osteotomy,” *Biomed Mater Eng.*, vol. 6(4), pp. 307–12, 1996.
- [33] “<https://www.crestremity.com/staples/>.” .
- [34] S. M. Russell, “Design considerations for nitinol bone staples,” *J. Mater. Eng. Perform.*, vol. 18, no. 5–6, pp. 831–835, 2009, doi: 10.1007/s11665-009-9402-1.
- [35] R. R. McKnight, S. K. Lee, and R. G. Gaston, “Biomechanical Properties of Nitinol Staples: Effects of Troughing, Effective Leg Length, and 2-Staple Constructs,” *J. Hand Surg. Am.*, vol. 44, no. 6, pp. 520.e1-520.e9, 2019, doi: 10.1016/j.jhsa.2018.08.017.
- [36] Q. C. J. Hoon, M. H. Pelletier, C. Christou, K. A. Johnson, and W. R. Walsh, “Biomechanical evaluation of shape-memory alloy staples for internal fixation—an in vitro study,” *J. Exp. Orthop.*, vol. 3, no. 1, 2016, doi: 10.1186/s40634-016-

- 0055-3.
- [37] C. C. Dock, K. L. Freeman, J. C. Coetzee, R. S. McGaver, and M. R. Giveans, “Outcomes of Nitinol Compression Staples in Tarsometatarsal Fusion,” *Foot Ankle Orthop.*, vol. 5, no. 3, p. 247301142094490, 2020, doi: 10.1177/2473011420944904.
- [38] E. Hornbogen, “Shape memory alloys,” *Prakt. Metallogr. Metallogr.*, vol. 26, no. 6, pp. 279–294, 1989, doi: 10.1227/01.neu.0000330392.09889.99.
- [39] I. Kauffman, G.B., Mayo, “The Story of Nitinol: The Serendipitous Discovery of the Memory Metal and Its Applications,” *Chem. Educ.* 2, 1–21, 1997.
- [40] K. Otsuka and X. Ren, “Physical metallurgy of Ti – Ni-based shape memory alloys,” vol. 50, pp. 511–678, 2005, doi: 10.1016/j.pmatsci.2004.10.001.
- [41] J. Nanotechnol, “Finite element analysis of thermally actuated medical stent and staple implants using shape memory alloy Mahyar Dahmardeh * and Seyed Kamaledin Setarehdan,” *Int. J. Nanotechnol.*, vol. 14, pp. 66–74, 2017.
- [42] A. Wadood, “Brief Overview on Nitinol as Biomaterial,” vol. 2016, 2016.
- [43] D. Stoeckel, “Nitinol medical devices and implants,” 2000.
- [44] T. Duerig, “An overview of nitinol medical applications,” 1999.
- [45] S. Recentering and T. Components, “Analytical Investigation of the Cyclic Behavior of,” 2017, doi: 10.3390/met7100386.
- [46] A. R. Pelton, J. DiCello, and S. Miyazaki, “Optimisation of processing and properties of medical grade Nitinol wire,” *Minim. Invasive Ther. Allied Technol.*, vol. 9, no. 2, pp. 107–118, 2000, doi: 10.3109/13645700009063057.
- [47] M. G. Ahlström, J. P. Thyssen, M. Wennervaldt, and J. D. Johansen, “Nickel allergy and allergic contact dermatitis: A clinical review of immunology , epidemiology , exposure , and treatment,” no. May, pp. 4–7, 2019, doi: 10.1111/cod.13327.
- [48] FDA-2019-D-1261, “Technical Considerations for Non- Clinical Assessment of Medical Devices Containing Nitinol - Guidance for Industry and Food and Drug Administration Staff,” no. 301. 2020.

- [49] J. F. L. Zhu, C. Trépanier, A. R. Peltron, “Oxidation of Nitinol and Its Effect on Corrosion Resistance.” ASM Materials & Processes for Medical Device Conference, 2003.
- [50] ASTM F564 – 17, “Standard Specification and Test Methods for Metallic Bone Staples.” .
- [51] F. Ben Hatira and K. Saidane, “A Thermo-Mechanical Behavior Simulation of A NiTi Staple Used for the Correction of Idiopathic Scoliosis,” *J. Biomater. Nanobiotechnol.*, vol. 03, no. 01, pp. 61–69, 2012, doi: 10.4236/jbnb.2012.31008.
- [52] A. F. Saleeb, B. Dhakal, and J. S. Owusu-Danquah, “Assessing the performance characteristics and clinical forces in simulated shape memory bone staple surgical procedure: The significance of SMA material model,” *Comput. Biol. Med.*, vol. 62, pp. 185–195, 2015, doi: 10.1016/j.compbiomed.2015.04.010.
- [53] O. Subasi, S. Torabnia, and I. Lazoglu, “In silico analysis of Superelastic Nitinol staples for trans-sternal closure,” *J. Mech. Behav. Biomed. Mater.*, vol. 107, no. February, 2020, doi: 10.1016/j.jmbbm.2020.103770.
- [54] D. Christ and S. Reese, “A finite element model for shape memory alloys considering thermomechanical couplings at large strains,” *Int. J. Solids Struct.*, vol. 46, no. 20, pp. 3694–3709, 2009, doi: 10.1016/j.ijsolstr.2009.06.017.
- [55] L. Krone *et al.*, “The potential of powder metallurgy for the fabrication of biomaterials on the basis of nickel-titanium: A case study with a staple showing shape memory behaviour,” *Adv. Eng. Mater.*, vol. 7, no. 7, pp. 613–619, 2005, doi: 10.1002/adem.200500029.
- [56] A. Aiyer, N. A. Russell, M. H. Pelletier, and W. R. Walsh, “The Impact of Nitinol Staples on the Compressive Forces, Contact Area, and Mechanical Properties in Comparison to a Claw Plate and Crossed Screws for the First Tarsometatarsal Arthrodesis,” *Foot Ankle Spec.*, vol. 9, no. 3, pp. 232–240, 2016, doi: 10.1177/1938640015620655.
- [57] N. A. Russell *et al.*, “Evaluation of Nitinol Staples for the Lapidus Arthrodesis in a Reproducible Biomechanical Model,” *Front. Surg.*, vol. 2, no. December, pp. 1–8, 2015, doi: 10.3389/fsurg.2015.00065.

- [58] <https://www.arthrex.com/>, “DynaNite® Nitinol Staple - Arthrex.” .
- [59] <https://abaqus-docs.mit.edu/>, “Superelasticity.” .
- [60] R. L. T. Auricchio, F., “Shape-Memory Alloys: Modeling and Numerical Simulations of the Finite-Strain Superelastic Behavior,” *Comput. Methods Appl. Mech. Eng.*, vol. 143, pp. 175–194, 1996.
- [61] R. L. T. Auricchio, F., “Shape-Memory Alloys: Macromodelling and Numerical Simulations of the Superelastic Behavior,” *Comput. Methods Appl. Mech. Eng.*, vol. 146, pp. 281–312, 1997.
- [62] M. A. Kleinstreuer, C., Li, Z., Basciano, C. A., Seelecke, S., Farber, “Computational mechanics of Nitinol stent grafts,” *J. Biomech.*, vol. 41(11), pp. 2370–2378, 2008, doi: doi: 10.1016/j.jbiomech.2008.05.032.
- [63] R. J. M. Pijpers and H. M. Slot, “Friction coefficients for steel to steel contact surfaces in air and seawater,” *J. Phys. Conf. Ser.*, vol. 1669, no. 1, 2020, doi: 10.1088/1742-6596/1669/1/012002.
- [64] and Z. L. Liberace R., “Mechanical Testing of Stainless Steel Bone Staples,” *J. Test. Eval.*, vol. 20, no. 3, pp. 217–224, 1992.
- [65] J. M. McNaney, V. Imbeni, Y. Jung, P. Papadopoulos, and R. O. Ritchie, “An experimental study of the superelastic effect in a shape-memory Nitinol alloy under biaxial loading,” *Mech. Mater.*, vol. 35, no. 10, pp. 969–986, 2003, doi: 10.1016/S0167-6636(02)00310-1.
- [66] M. J. Mahtabi, N. Shamsaei, and M. R. Mitchell, “Fatigue of Nitinol: The state-of-the-art and ongoing challenges,” *Journal of the Mechanical Behavior of Biomedical Materials*, vol. 50, pp. 228–254, 2015, doi: 10.1016/j.jmbbm.2015.06.010.
- [67] FDA-2019-D-1261, “Technical Considerations for Non- Clinical Assessment of Medical Devices Containing Nitinol - Guidance for Industry and Food and Drug Administration Staff,” no. 301, 2020.
- [68] A. R. Pelton, “Nitinol fatigue: A review of microstructures and mechanisms,” *J. Mater. Eng. Perform.*, vol. 20, no. 4–5, pp. 613–617, 2011, doi: 10.1007/s11665-

- 011-9864-9.
- [69] M. B. Pelton, A.R., V. Schroedera, M.R. Mitchellb, Xiao-Yan Gongc and S. W. Robertsond, “Fatigue and durability of Nitinol stents,” *J. Mech. Behav. Biomed. Mater.*, vol. 1, pp. 153–164, 2008.
- [70] G. Scalet, C. Menna, A. Constantinescu, and F. Auricchio, “A computational approach based on a multiaxial fatigue criterion combining phase transformation and shakedown response for the fatigue life assessment of Nitinol stents,” *J. Intell. Mater. Syst. Struct.*, vol. 29, no. 19, pp. 3710–3724, 2018, doi: 10.1177/1045389X18798957.
- [71] R. R. McKnight, S. K. Lee, and R. G. Gaston, “Biomechanical Properties of Nitinol Staples: Effects of Troughing, Effective Leg Length, and 2-Staple Constructs,” *J. Hand Surg. Am.*, vol. 44, no. 6, pp. 520.e1-520.e9, 2019, doi: 10.1016/j.jhsa.2018.08.017.
- [72] E. Dordoni, L. Petrini, W. Wu, F. Migliavacca, G. Dubini, and G. Pennati, “Computational Modeling to Predict Fatigue Behavior of NiTi Stents: What Do We Need?,” *J. Funct. Biomater.*, vol. 6, no. 2, pp. 299–317, 2015, doi: 10.3390/jfb6020299.
- [73] R. Marrey *et al.*, “Validating fatigue safety factor calculation methods for cardiovascular stents,” *J. Biomech. Eng.*, vol. 140, no. 6, pp. 1–29, 2018, doi: 10.1115/1.4039173.
- [74] K. W. Morrison T. M., M. L. Dreher M. L., Nagaraja S., Angelone L. M., “The Role of Computational Modeling and Simulation in the Total Product Life Cycle of Peripheral Vascular Devices,” *J Med Device*, vol. 176, no. 12, pp. 139–148, 2017, doi: 10.1115/1.4035866.
- [75] T. M. Morrison, P. Pathmanathan, M. Adwan, and E. Margerrison, “Advancing regulatory science with computational modeling for medical devices at the FDA’s office of science and engineering laboratories,” *Front. Med.*, vol. 5, no. SEP, pp. 1–11, 2018, doi: 10.3389/fmed.2018.00241.